NEUROSCIENCE

A striosomal accumbens pathway drives stereotyped behavior through an aversive Esr1+ hypothalamic-habenula circuit

Thomas Contesse[1], Buse Yel Bektash[1], Marta Graziano[1], Chiara Forastieri[1], Alessandro Contestabile[1], Salome Hahne[2], Felix Jung[1], Ifigeneia Nikolakopoulou[1], Eleonora Rubino[1], Xiao Cao[1], Vasiliki Skara[1], Ioannis Mantas[1], Sarantis Giatrellis[2], Marie Carlén[1], Rickard Sandberg[2], Daniela Calvigioni[1]*, Konstantinos Meletis[1]*

The lateral hypothalamic area (LHA) integrates external stimuli with internal states to drive the choice between competing innate or value-driven motivated behaviors. Here, we define a striosomal Tac1+/Tshz1+/Oprm1+ neuron subtype in the nucleus accumbens (ACB) that targets Esr1+ LHA neurons that project to the lateral habenula (LHb). Intersectional cell type–specific and input-output defined optogenetic activation of this ACB-LHA-LHb pathway can progressively induce a negative behavioral state that depends on Esr1+ LHA-LHb neural activity. We found that either activation of the D1+ ACB-LHA projection or inhibition of LHA-LHb neurons defined by ACB inputs can drive reward-independent compulsive-like behaviors that generalize across contexts. We found that these complex yet stereotyped behaviors compete with highly motivated states and can override the drive for natural rewards or social interactions. Our findings reveal a discrete Tac1+ striosomal ACB projection targeting the aversive Esr1+ LHA-LHb pathway as a key circuit that promotes stereotyped and compulsive-like behaviors over goal-directed actions.

INTRODUCTION

Animals must flexibly adapt their behavior in response to contextual cues and homeostatic signals, balancing goal-directed actions with exploration or foraging, as well as expressing complex innate behaviors such as grooming and social interactions (*1*, *2*). The hypothalamic circuitry plays a central role in the dynamic competition between behavioral states and actions by integrating external stimuli and internal states to support appropriate behaviors (*3*). Suppression of repetitive and nonrewarded actions is essential for maintaining appropriate context-dependent responses, and impairments in the ability to flexibly adapt behaviors are central to compulsivity and stereotypies. The hypothalamic circuitry has been implicated in conditions where maladaptive and compulsive behaviors are prominent, such as obesity, anorexia, obsessive-compulsive disorder (OCD), and addiction (*4*).

The hypothalamus is spatially organized and composed of a large number of neuron subtypes (*5*–*8*). Within the hypothalamus, neurons in the lateral hypothalamic area (LHA) directly control motivational states and behavioral programs essential for maintaining energy homeostasis (e.g., feeding) (*9*). GABAergic and glutamatergic neurons in the LHA have been identified as having opposing roles in regulating feeding behaviors, with GABAergic neurons promoting feeding and glutamatergic neurons inhibiting it (*10*). LHA neurons that drive feeding have also been linked to compulsive and stereotyped actions, for example, Agrp-expressing neurons, which were first identified as central regulators of hunger signals (*11*), can additionally promote the expression of compulsive or stereotyped behaviors (*12*).

The general role of LHA neurons in motivated behaviors has been established, yet it remains unknown how circuit-specific inputs and outputs of LHA neuron subtypes shape the balance and competition between behavioral states. The integration of internal homeostatic signals with value prediction signals and external stimuli depends on projection of hypothalamic signals to downstream circuits. For example, LHA glutamatergic projections to the ventral tegmental area (VTA) control reward and compulsive seeking without affecting food consumption (*10*) and have a role in stress-induced overfeeding (*13*). Instead, the LHA glutamatergic neurons projecting to the lateral habenula (LHb), a hub for processing aversive stimuli and negative reinforcement, control negative states and feeding (*14*–*17*). The identity and function of the glutamatergic LHA-LHb neurons are complex (*18*), with the subtype expressing estrogen receptor 1 (Esr1) being central for aversive signaling and in negative stress-related states (*19*). Glutamatergic neurons in the LHA receive inputs from the bed nuclei of stria terminalis (BST) that can suppress feeding and promote aversion (*20*). Another major source of inputs to the LHA comes from D1+ neurons in the nucleus accumbens (ACB) that target GABAergic as well as glutamatergic neurons to control feeding (*21*, *22*).

To study the circuit mechanisms in the LHA that control the competition between aversive states and the expression of goal-directed actions, we investigated organization and function of the cell type–specific inputs to the aversive LHA neuron subtype that is defined by expression of the Esr1 and projections to the LHb (Esr1+ LHA-LHb neurons). We mapped the identity of the whole-brain synaptic inputs to Esr1+ LHA-LHb neurons using neuroanatomical and single-neuron RNA sequencing profiling and performed circuit-specific manipulation during naturalistic and motivated behaviors. In summary, our findings establish the organization and identity of a striosomal Tac1+/Tshz1+ ACB-LHA projection that drives reward-independent compulsive-like behaviors.

[1]Department of Neuroscience, Karolinska Institutet, Stockholm, Sweden. [2]Department of Cell and Molecular Biology, Karolinska Institutet, Stockholm, Sweden.
*Corresponding author. Email: daniela.calvigioni@ki.se (D.C.); dinos.meletis@ki.se (K.M.)

RESULTS

Characterization of monosynaptic inputs to the Esr1+ LHA-LHb pathway

We first used a strategy to map the cell type–specific monosynaptic inputs to the LHA neuron subtype defined by its projections to LHb and expression of Esr1 (Esr1+ LHA-LHb neurons), using a genetically modified rabies virus for whole-brain input tracing (*23*, *24*). We injected an adeno-associated virus (AAV) with cre-dependent expression of the TVA receptor and the rabies glycoprotein (RG) into the LHA of Esr1-cre mice followed by injection of the EnvA-coated green fluorescent protein (GFP)–expressing rabies virus into LHb (Fig. 1, A and B). On the basis of the GFP labeling of the whole-brain monosynaptic

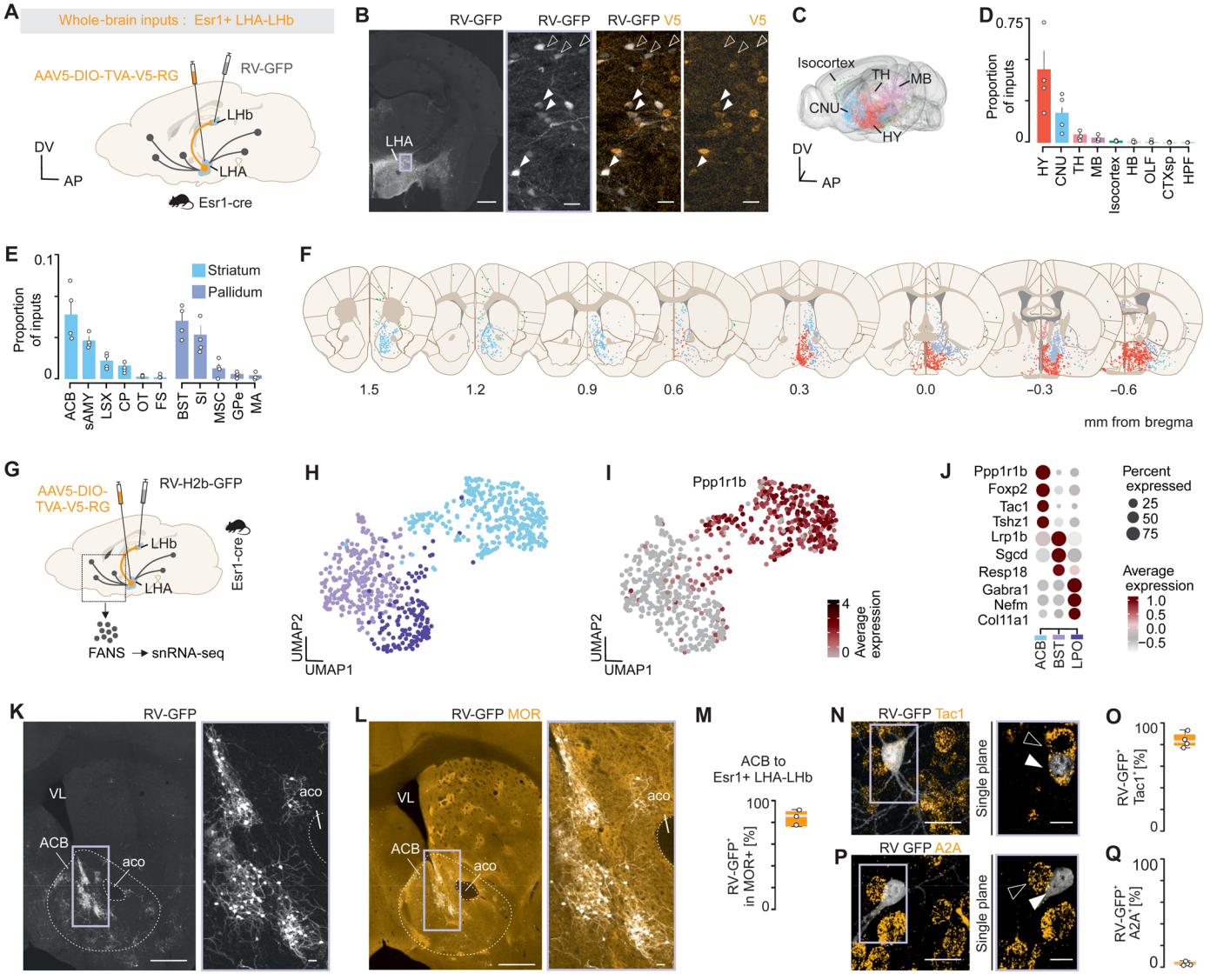

Fig. 1. Characterization of the monosynaptic inputs to the Esr1+ LHA-LHb pathway. (**A**) Experimental strategy for rabies tracing of Esr1+ LHA-LHb inputs. The helper virus (AAV5-DIO-TVA-V5-RG) was injected in the LHA and the EnvAcoated rabies virus (RV-GFP) in the LHb. (**B**) Representative confocal images of starter neurons coexpressing RV-GFP (white) and V5 (orange; arrowheads: RV-GFP+/V5+ neurons; empty arrowheads: RV-GFP+/V5− neurons). (**C**) Whole-brain visualization of RV-GFP+–labeled neurons (color coded by neuroanatomical region; 21,742 neurons, $n = 1$). (**D** and **E**) Quantification of inputs per brain region ($n = 4$ mice). (**F**) Coronal plates (Allen Brain Atlas CCFv2) showing detected GFP+ input neurons (one dot, one neuron; each plate shows neurons detected in two consecutive brain sections from one representative mouse). (**G**) Rabies tracing strategy and workflow for snRNA-seq of inputs to Esr1+ LHA-LHb neurons. (**H**) UMAP plot showing clustering of neurons based on their transcriptional profile (1093 nuclei, average 4744.375 genes per neurons). (**I**) Visualization of the striatal marker Ppp1r1b in the UMAP plot. (**J**) Average expression of selected cell type markers per cluster. (**K**) Representative confocal images of ACB inputs to Esr1+ LHA-LHb (GFP in white). (**L**) Same image as in (K), showing MOR expression (orange). (**M**) RV-GFP+ ACB neurons overlapping with MOR expression. (**N**) Representative confocal images showing Tac1 expression (orange) in ACB RV-GFP+ neurons (white; arrowheads: RVGFP+/Tac1+ neurons; empty arrowheads: RV-GFP−/Tac1+ neurons). (**O**) Quantification of Tac1 expression in RV-GFP+ ACB neurons. (**P**) Representative confocal images showing A2A expression (orange) in ACB RV-GFP+ neurons (white; arrowheads: RV-GFP+/A2A+ neurons; empty arrowheads: RV-GFP−/A2A+ neurons). (**Q**) Quantification of A2A expression in RV-GFP+ ACB neurons. Scale bars, 500 μm [(B) left, (K) left, and (L) left] and 20 μm [(B) right, (K) right, (L) right, (N), and (P)].

inputs, we quantified the input populations following the region definitions in the Allen mouse brain reference atlas (Fig. 1C and fig. S1, A to K). We found that the largest number of labeled inputs were found locally within the hypothalamus, whereas the largest number of long-range inputs were found in the cerebral nuclei (Fig. 1D). We further analyzed the distribution of the labeled inputs in the cerebral nuclei and found that the largest proportion of labeled inputs was localized in the ACB, followed by the striatum-like amygdalar nuclei (sAMY), and for the pallidum, in the BST and the substantia innominata (SI) (Fig. 1, E and F).

To identify the molecular profile of neurons subtypes with inputs to Esr1+ LHA-LHb neurons, we labeled the monosynaptic inputs using a nuclear-localized GFP (H2b-GFP)–expressing rabies virus followed by sorting of single GFP+ nuclei and single-nucleus RNA sequencing (snRNA-seq) (Fig. 1G). Analysis of the snRNA-seq data revealed that the input populations clustered into three main groups, with the largest cluster consisting of Ppp1r1b+ neurons (Fig. 1, H and I). The Ppp1r1b+ cluster confirmed that the major input to Esr1+ LHA-LHb neurons came from striatal projection neurons, and we therefore further analyzed cell type markers in the striatal cluster. We found that ACB neurons with monosynaptic inputs to Esr1+ LHA-LHb neurons were defined by expression of several striatal neuron subtype markers (e.g., Foxp2, Tac1, and Tshz1; Fig. 1J and figs. S2, A to D, and S3, A to C), which supported the notion that ACB projections to Esr1+ LHA-LHb neurons are formed by a discrete Ppp1r1b+/Tac1+/Tshz1+ pathway.

On the basis of the expression of the striosome-enriched markers Tac1 and Tshz1 in the ACB subpopulation, we imaged the spatial organization of the rabies-labeled neurons, which revealed a characteristic striosomal type organization, with GFP+-labeled neurons being colocalized with the dense mu opioid receptor (MOR) staining (Fig. 1, K to M, and fig. S3, D to G). To further profile the GFP+-labeled ACB neurons, we performed in situ hybridization for the two main neuron types in the ACB, namely, the D1 and D2 receptor–expressing neurons, using Tac1 and A2A expression as cell type markers. We found that 85% of the GFP+-labeled ACB neurons could be classified as Tac1+ neurons (Fig. 1, N to Q). In summary, using brainwide monosynaptic rabies tracing together with snRNA-seq and neuron type profiling, we identified that the Esr1+ LHA-LHb neurons receive a major input from Tac1+/Tshz1+/Oprm1+ striosomal type ACB neurons.

Neuroanatomical mapping of a cell type–specific ACB-LHA-LHb circuit

To directly visualize the distribution of the striosomal type ACB synaptic terminals in the hypothalamus, we injected an AAV enabling cre-dependent expression of tdTomato together with a synaptophysin-localized GFP fusion protein (SYP-GFP) into the ACB of D1-cre or Oprm1-cre mice (Fig. 2, A to C, and figs. S3H and S4A). For both D1+ as well as Oprm1+ ACB neurons, we mapped the localization of SYP-GFP–expressing axon terminals (fig. S4B) and found them concentrated to a specific domain in the LHA, which was consistent with the canonical location of the Esr1+ LHA-LHb population (*19*) (Fig. 2, D to G). To further confirm the cell type–specific organization of the LHA-LHb neurons receiving ACB inputs, we designed an intersectional input-output somatic mapping strategy to genetically label neurons that receive inputs from ACB and that also project to LHb. We used an anterograde transsynaptic mapping strategy based on AAV1 injection (AAV1-Cre) into the ACB to label the postsynaptic targets of the ACB neurons, in combination with labeling of the LHb-projecting neurons using injections of retrogradely transported cre-dependent AAV (AAVretro-DIO-tdTomato) into the LHb (Fig. 2H). Our intersectional input-output mapping strategy resulted in the genetic labeling specifically of the LHA-LHb neurons that receive direct ACB inputs (Fig. 2I and fig. S4C). This labeling strategy showed that the LHA-LHb subpopulation was topographically distributed in an LHA domain that overlaps with the densest axonal projections from D1+ and Oprm1+ ACB neurons, and most labeled neurons expressed Esr1 (Fig. 2, J to L). To directly visualize the axonal projection in the LHb of Esr1+ LHA neurons that receive inputs from ACB, we used a different input-output axonal mapping strategy. We injected transsynaptic AAV1-flpo into the ACB and a cre-dependent/flpo-dependent vector for expression of ChR2 (AAV8-Con/Fon-hChR2-YFP) into the LHA of Esr1-cre mice (Fig. 2M). This strategy resulted in the genetic expression of ChR2–yellow fluorescent protein (YFP) in Esr1+ LHA neurons with specific inputs from ACB and visualization of their axon terminals in the LHb (Fig. 2N). We found that Esr1+ LHA-LHb neurons receiving ACB inputs showed a spatially organized axonal targeting within the LHb, with a preferential targeting of the medial domain of the LHb (Fig. 2O). In summary, we established intersectional input-output mapping strategies to target Esr1+ LHA-LHb neurons receiving ACB inputs and mapped their organization in the LHA as well as their discrete target domain in the LHb.

Repeated activation of D1+ ACB-LHA projection neurons drive aversion through the Esr1+ LHA-LHb pathway

To investigate how modulation of aversive states depends on the integration of the ACB inputs on the Esr1+ LHA-LHb pathway, we first tested the aversive signaling of LHA-LHb neurons that are genetically defined by Esr1+ expression and ACB inputs. To specifically target the Esr1+ LHA-LHb neurons with direct inputs from ACB, we used an intersectional input-output strategy in Esr1-cre mice, based on transsynaptic anterograde AAV1 labeling to express flpo recombinase only in neurons that receive ACB inputs, together with injection into the LHA of the flpo-dependent and cre-dependent ChR2 vector (AAV8-Con/Fon-ChR2-YFP). With this intersectional strategy, we expressed ChR2 in Esr1+ LHA neurons targeted by the ACB and selectively stimulated LHb terminals with optical fibers placed on top of the LHb (Fig. 3A and fig. S5). We used a real-time place avoidance test to quantify the ChR2-induced aversive signals, with a first exposure (10 min) of optogenetic activation in one compartment, followed by a second exposure (10 min) where the optogenetic activation was switched to the opposite compartment (Fig. 3B). We found that both male and female mice strongly avoided the compartment with the ChR2-induced activation of the ACB-targeted Esr1+ LHA-LHb terminals in the first exposure as well as after switching compartment stimulation without affecting locomotor activity (Fig. 3C and fig. S6, A to C). This result confirmed our prediction that Esr1+ LHA-LHb neurons with specific ACB inputs drive strongly aversive signals. To assess the function of ACB inputs to LHA in modulating aversive states, we used two different viral strategies for optogenetic activation of ACB terminals that target the LHA as well as the cell type–specific activation of the D1+ ACB-LHA projection neurons (Fig. 3, D and E). In the first strategy, we injected the retrogradely transported herpes simplex virus (HSV) into LHA to express cre recombinase (HSV-cre-mCherry) in neurons projecting to LHA and a cre-dependent

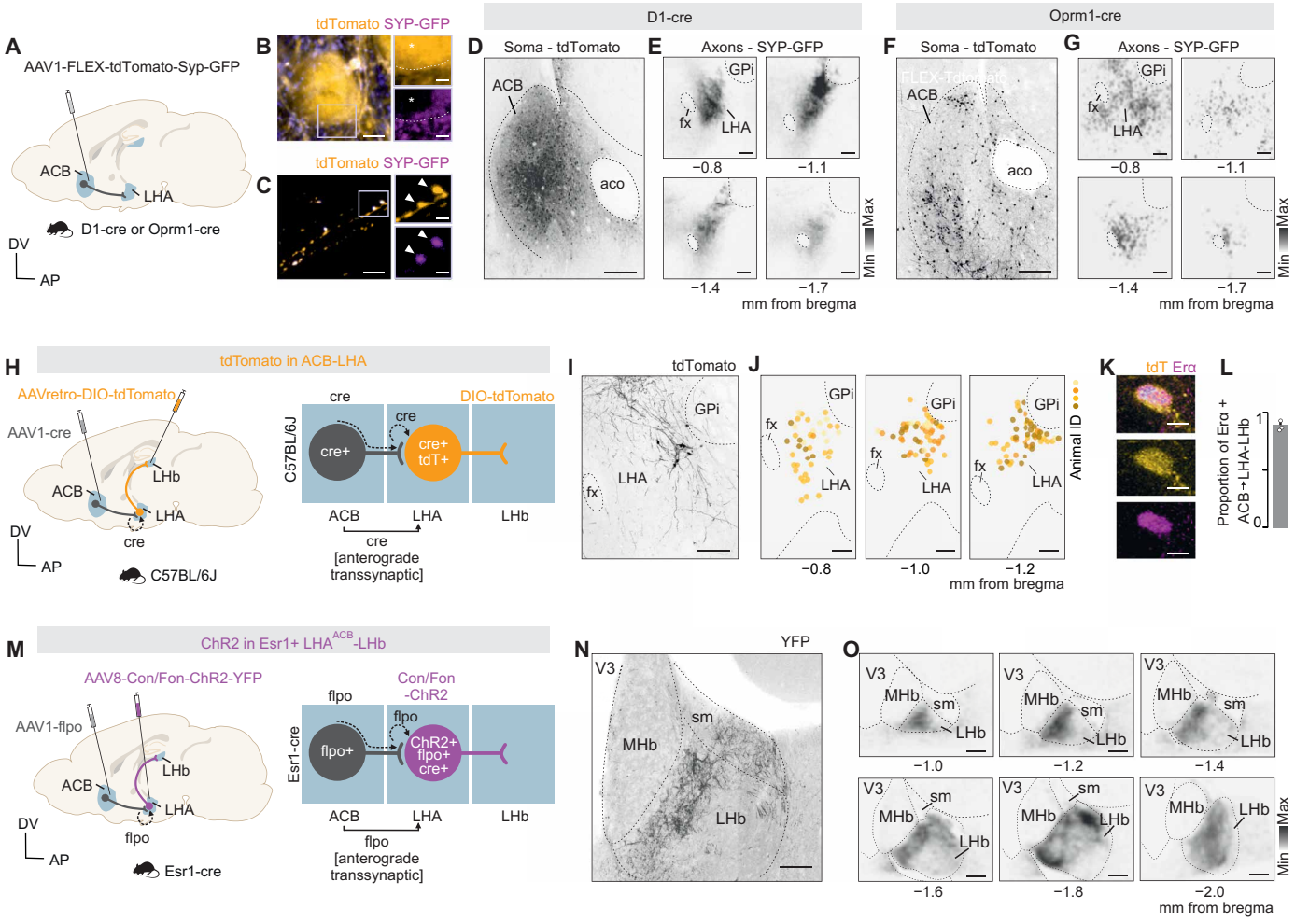

Fig. 2. Neuroanatomical mapping of a cell type–specific ACB-LHA-LHb circuit. (**A**) Viral strategy for cell type–specific labeling of ACB-LHA axon terminals. (**B** and **C**) Representative confocal images showing the expression of tdTomato (orange) in soma [(B), soma in the ACB] and axons [(C), axons in the LHA] and SYP-GFP to presynaptic terminals (purple; light purple boxes: location of right panels; asterisk: tdTomato+ soma; arrowheads: ACB-LHA tdTomato+/SYP-GFP+ presynaptic terminal). (**D**) Representative confocal image of tdTomato expression in ACB D1+ neurons. (**E**) Heatmaps of ACB D1+ axon terminal distribution in the LHA (black, SYP-GFP+). (**F**) Representative confocal image of tdTomato expression in ACB Oprm1+ neurons. (**G**) Heatmaps of ACB Oprm1+ axon terminal distribution in the LHA (black, SYP-GFP+). (**H**) Experimental strategy for ACB-input and LHb-output specific labeling of LHA neurons. (**I**) Representative confocal image of transsynaptic labeling of LHA-LHb neurons with ACB inputs. (**J**) Coronal plates showing the position of detected LHA-LHb neurons with ACB inputs ($n = 4$ mice; one color, one mouse; one dot, one neuron). (**K**) Representative confocal image showing Erα protein expression in LHA-LHb neurons with ACB inputs (tdTomato, orange; Erα, purple). (**L**) Quantification of Erα expression in LHA-LHb neurons with ACB inputs. (**M**) Experimental strategy transsynaptic labeling of Esr1+ LHA-LHb neurons with ACB inputs and expression of ChR2. (**N**) Representative confocal image showing labeling of axon terminals in the LHb from Esr1+ LHA-LHb neurons with ACB inputs. (**O**) Heatmaps of axon terminal distribution in the LHb from Esr1+ LHA neurons with ACB inputs (black, SYP-GFP+). Scale bars, 300 μm [(D) and (F)], 250 μm (I), 100 μm [(E), (G), (J), (N), and (O)], 10 μm (K), 2 μm [(B) left and (C) left], and 1 μm [(B) right and (C) right].

ChR2-expressing vector into ACB (AAV5-DIO-ChR2-YFP), resulting in a selective targeting of LHA projecting ACB neurons. In the second strategy, we targeted D1+ projection neurons in the ACB using local injection of a cre-dependent ChR2-expressing vector in D1-cre mice (AAV5-DIO-ChR2-mCherry) and stimulated their axon terminals through optical fibers placement in the LHA. In contrast to the immediate avoidance induced by direct stimulation of the Esr1+ LHA-LHb pathway, we found that activation of the inhibitory ACB inputs in the LHA did not immediately induce preference or avoidance for the ChR2-stimulated compartment in the real-time place avoidance test. In response to the second exposure and repeated ChR2 stimulation, we found an increased and significant avoidance to the ChR2-stimulated compartment (Fig. 3, F and G). These results together suggest that activation of the D1+ ACB terminals in the LHA does not produce an immediate place preference through inhibition of the LHA-LHb pathway but, after repeated activation, instead induces an aversive state. We therefore asked whether the negative state induced by repeated optogenetic activation of ACB-LHA neurons depended on recruitment of the Esr1+ LHA-LHb pathway. To test this hypothesis, we used an intersectional input-output strategy that allowed us to perform optogenetic stimulation of the ACB-LHA projections together with cell type–specific silencing of Esr1+ LHA-LHb neurons using tetanus light chain (TeLC) expression. We targeted the ACB neurons that

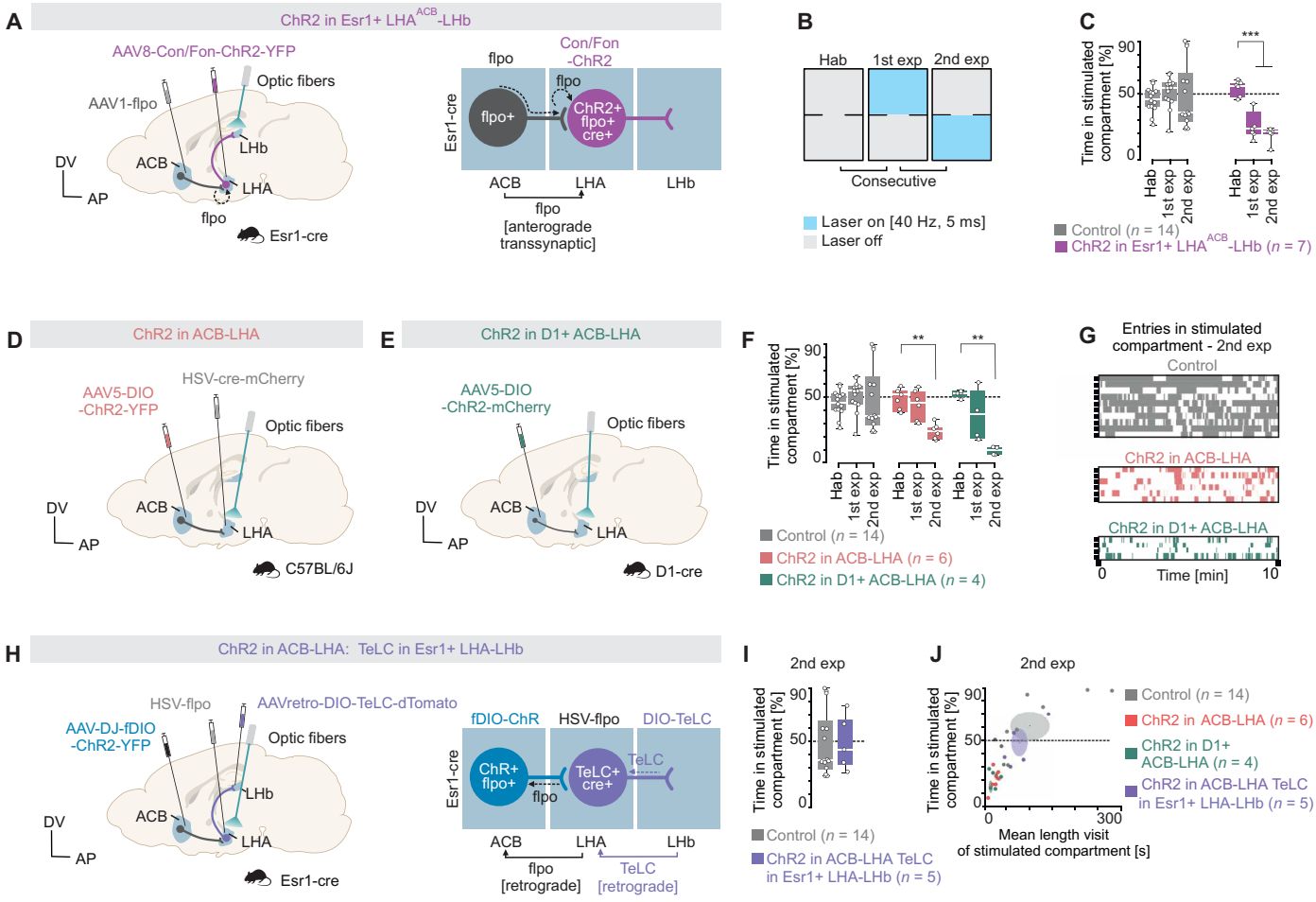

Fig. 3. Repeated activation of D1+ ACB-LHA projection neurons drive aversion through the Esr1+ LHA-LHb pathway. (**A**) Experimental strategy for optogenetic terminal stimulation of Esr1+ LHA-LHb neurons with direct ACB inputs (ChR2 in Esr1+ LHA^{ACB}-LHb). (**B**) Schematic of the real-time place avoidance test. (**C**) Optogenetic activation of the Esr1+ LHA^{ACB}-LHb pathway decreased time spent in the stimulated compartment during first and second exposure of the real-time place avoidance test (two-way ANOVA, $P = 0.0055$, ChR2 in Esr1+ LHA^{ACB}-LHb Hab versus 1st exp: $P = 0.0006$, ChR2 in Esr1+ LHA^{ACB}-LHb Hab versus 2nd exp: $P < 0.0001$). (**D**) Strategy for pathway-specific optogenetic activation of ACB-LHA axon terminals (ChR2 in ACB-LHA). (**E**) Strategy for cell type–specific optogenetic activation of D1+ ACB-LHA axon terminals (ChR2 in D1+ ACB-LHA). (**F**) Optogenetic activation of D1+ ACB-LHA or ACB-LHA pathways induced an avoidance of the stimulated compartment during the second exposure in the real-time place avoidance test (two-way ANOVA, $P = 0.0171$, ChR2 in ACB-LHA hab versus 2nd exp: $P = 0.0095$, ChR2 in D1+ ACB-LHA hab versus 2nd exp: $P = 0.0012$). (**G**) Visualization of entries to stimulated compartment (one color-coded vertical bar, 1 s in the stimulated compartment). (**H**) Strategy for optogenetic activation of the ACB-LHA pathway combined with TeLC silencing of the Esr1+ LHA-LHb neurons (ChR2 in ACB-LHA: TeLC in Esr1+ LHA-LHb). (**I** and **J**) Optogenetic activation of the ACB-LHA pathway together with TeLC silencing of the Esr1+ LHA-LHb pathway normalized the mean duration and number of visits to the stimulated compartment. See table S5 for more details on the statistical analyses performed here.

project to the LHA using an HSV-based retrograde expression of flpo (HSV-flpo in the LHA) combined with a local injection of the flpo-dependent ChR2 in the ACB (AAV-DJ-fDIO-ChR2-YFP) in Esr1-cre mice. We combined this projection-specific ChR2 expression with cell type–specific silencing of the Esr1+ LHA-LHb neurons using injection into LHb of a retrograde vector with cre-dependent TeLC expression (AAVretro-DIO-TeLC-dTomato) (Fig. 3H and fig. S4, D to F). We found that the cell type–specific silencing of the Esr1+ LHA-LHb neurons completely blocked the avoidance response of repeated activation of ACB-LHA projections (Fig. 3I). More specifically, this silencing approach led to an overall increase in both the total time spent in the paired compartment and the average duration of each visit, reaching levels comparable to those of the control group (Fig. 3J). In summary, we found that the D1+ ACB-LHA pathway shapes the transition to an aversive state after repeated activation and that this negative state depends on recruitment of the Esr1+ LHA-LHb neurons.

The D1+ ACB-LHA pathway drives a compulsive-like digging state

Following our findings on the negative state induction after repeated activation of the ACB-LHA pathway in the place avoidance assay, we aimed to define how activation affected the expression of discrete exploratory or motor motifs. Using an elevated plus maze and an open field test, we first found that the negative state induced by activation of the ACB-LHA was not associated with higher anxiety levels in mice (fig. S6, D and E). We decided next to capture the detailed behavioral changes imposed by activation of the D1+ ACB-LHA

pathway using automated tracking and pose estimation in an open field environment using DeepLabCut [DLC (*25*)] and classified behavioral motifs using an unsupervised probabilistic deep learning model [Variational Autoencoders for Motif Extraction (VAME) (*26*)] (Fig. 4A and fig. S6F). We found that, in both male and female mice, repeated optogenetic activation of D1+ ACB-LHA terminals resulted in a significant increase in locomotor speed (Fig. 4B, fig. S6, H and I, and table S1) and shifted the behavioral repertoire toward vigorous exploratory motifs (Fig. 4, C to E; fig. S6G; and table S2) such as rearing and fast turning (e.g., motif 3: "walking followed by standing"; motif 33: "walking followed by sharp clockwise turning").

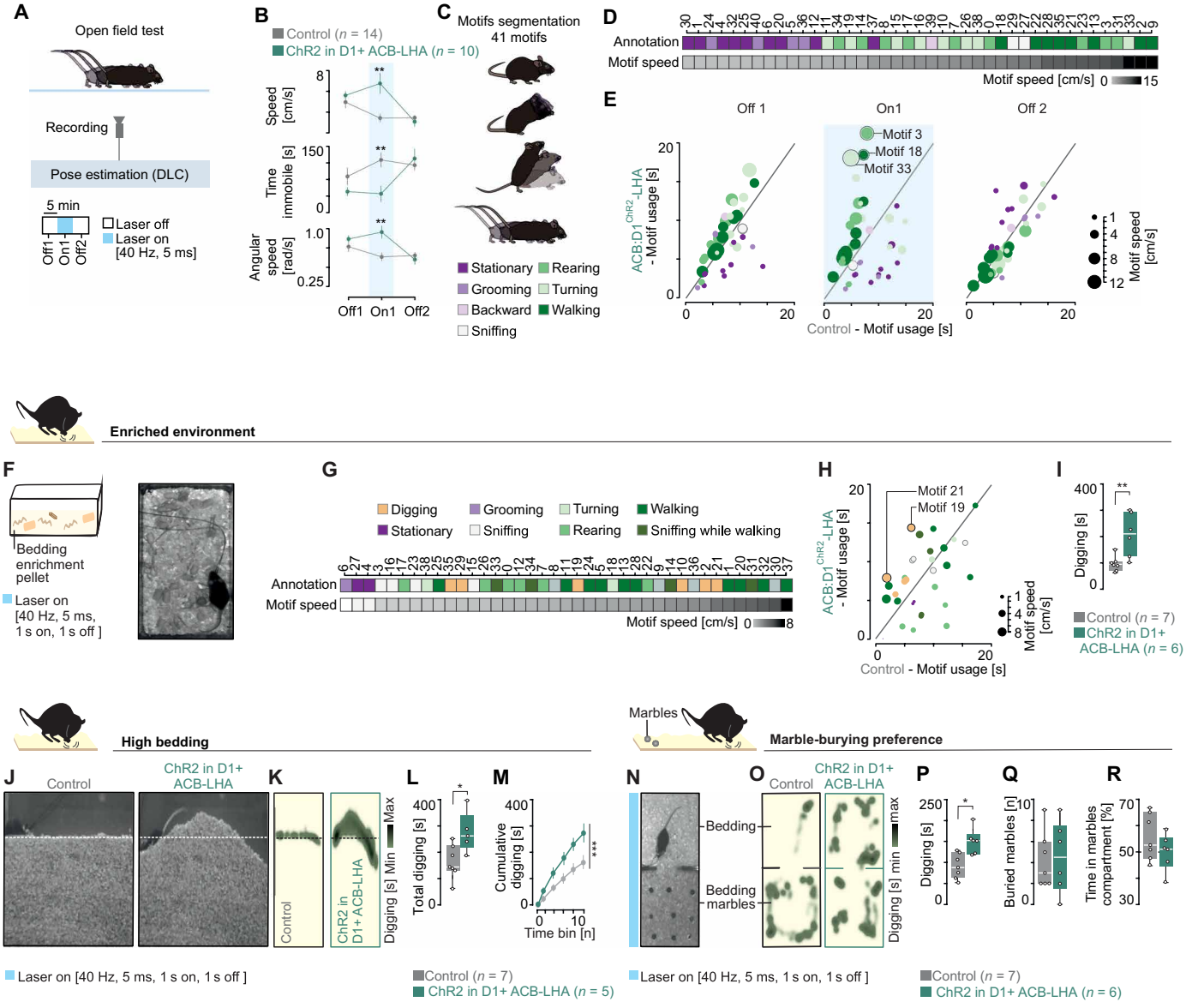

Fig. 4. The D1+ ACB-LHA pathway drives a compulsive-like digging state. (**A**) Schematic of the open field test. (**B**) Optogenetic activation of the D1+ ACB-LHA pathway increased locomotor and angular speed while decreasing immobility during the open field test (Mann-Whitney, speed: $P = 0.008$, time immobile: P On1 $= 0.007$, angular speed: $P = 0.003$). (**C**) Schematic of motifs segmented using Variational Autoencoders for On1 Motif Extraction (VAME). (**D**) Behavioral classification and relative speed of the 41 motifs found with VAME during exploration of an open field arena. (**E**) Visualization of motif usage during optogenetic activation of the D1+ ACB-LHA pathway versus control. Each motif is represented with a point (color, behavioral classification; size, motif speed). (**F**) Schematic and image of the enriched home cage assay. (**G**) Behavioral classification and relative speed of the 39 motifs found in the enriched home cage assay. (**H**) Visualization of motif usage during optogenetic activation of the D1+ ACB-LHA pathway versus control during enriched home cage assay. (**I**) Optogenetic activation of the D1+ ACB-LHA pathway increased the time spent digging enriched home cage environment (Mann-Whitney, $P = 0.0041$). (**J**) Schematic and image of the high bedding assay. (**K**) Heatmaps of the digging location in the arena. (**L** and **M**) Optogenetic activation of the D1+ ACB-LHA pathway increased the digging behavior across the entire session (Mann-Whitney, $P = 0.0303$) (two-way ANOVA, $P < 0.0009$). (**N**) Image of the two-compartment marble-burying assay. (**O**) Heatmaps of the digging location in the two compartments of the arena. (**P** to **R**) Optogenetic activation of the ACB-LHA pathway increased the digging behavior but not directed toward the marbles (Mann-Whitney, $P = 0.014$). See table S5 for details on the statistical analyses.

We next asked whether these behavioral motifs represented a complex negative state that would generalize to an enriched environment. Therefore, we optogenetically activated the D1+ ACB-LHA axon terminals in an enriched environment with natural bedding material and freely available food (pellets; Fig. 4F). Unexpectedly, activation of the D1+ ACB-LHA axon terminals in the presence of bedding material resulted in vigorous digging behavior and decreased rearing in female and male mice (Fig. 4, G to I; fig. S6, J to S; and table S3).

We next performed the same ACB-LHA activation paradigm in a context designed to promote exploratory and digging behavior using a high bedding assay (Fig. 4J). In this context, we found that mice showed a strong and sustained digging behavior during the entire period of optogenetic activation of the D1+ ACB-LHA axons (Fig. 4, K to M; fig. S7A; and movie S1). We next asked whether the sustained digging behavior represented a goal-directed or purposeful action or was the expression of a compulsive-like response. For this, we performed a modified place-preference test where bedding material was present in both compartments whereas marbles were paired with only one (Fig. 4N). Optogenetic stimulation of D1+ ACB-LHA terminals induced a specific and significant increase in digging behavior irrespective of the marble-paired compartment, without changing the number of buried marbles or the time spent in the marble-paired compartment (Fig. 4, O to R, and fig. S7, B and C). In summary, we found that the activation of a discrete D1+ ACB-LHA pathway leads to sustained and compulsive-like seeking or digging behavior that was not directed toward salient objects (e.g., marbles).

The D1+ ACB-LHA pathway suppresses competing motivational states to drive compulsive-like seeking

We further aimed to define how competing high-motivational states, such as feeding and social interaction, could affect the expression of the induced compulsive-like seeking behavior. To determine the competition with feeding programs, we activated the D1+ ACB-LHA pathway in food-deprived mice in a modified two-compartment assay with bedding in both compartments and freely accessible food (pellet) in only one compartment (Fig. 5A). In this assay, hungry mice with optogenetic activation of the D1+ ACB-LHA pathway showed a complete suppression of feeding behavior. Notably, feeding behavior was restored when the optogenetic activation ended (Fig. 5, B and C). The reduced feeding behavior was not coupled to avoidance of the food-paired compartment (Fig. 5, D and E) or with change of locomotor speed (fig. S7D). Instead, we found that the D1+ ACB-LHA activation induced a significant rapid increase in digging behavior in both compartments (Fig. 5, F to H). Last, we assessed whether

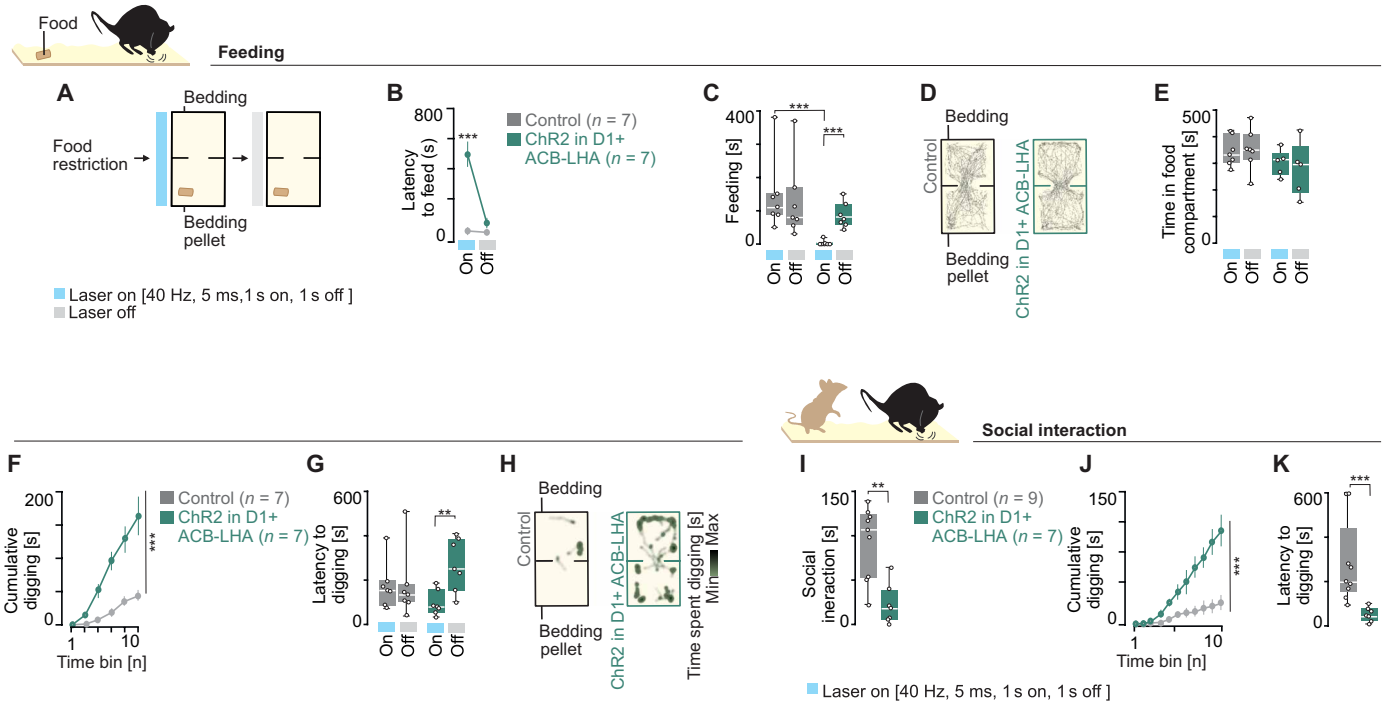

Fig. 5. The D1+ ACB-LHA pathway suppresses competing motivational states to drive compulsive-like seeking. (**A**) Schematic of the two-compartment feeding test. (**B** and **C**) Optogenetic activation of the D1+ ACB-LHA pathway suppressed feeding behavior (two-way ANOVA, $P < 0.0001$) (Mann-Whitney, control On versus ChR2 in D1+ ACB-LHA On: $P = 0.0006$; ChR2 in D1+ ACB-LHA On versus ChR2 in D1+ ACB-LHA Off: $P = 0.0006$). (**D**) Example of mouse tracking in the two-compartment food test. (**E**) Optogenetic activation of the D1+ ACB-LHA pathway did not change the time spent in the food-paired compartment. (**F**) Optogenetic activation of the D1+ ACB-LHA pathway increased the digging behavior across the entire session in the two-compartment food test (two-way ANOVA, $P < 0.0001$). (**G**) Optogenetic activation of the D1+ ACB-LHA pathway decreased the latency to first digging behavior in the two-compartment food test (Mann-Whitney, ChR2 in D1+ ACB-LHA On versus ChR2 in D1+ ACB-LHA Off: $P = 0.007$). (**H**) Heatmaps showing digging in the two-compartment food test. (**I**) Optogenetic activation of the D1+ ACB-LHA pathway decreased social interaction time (Mann-Whitney, $P = 0.0024$). (**J**) Optogenetic activation of the D1+ ACB-LHA pathway increased the digging behavior across the entire session (two-way ANOVA, $P < 0.0001$). (**K**) Optogenetic activation of the D1+ ACB-LHA pathway decreased latency for first digging behavior in the social interaction test (Mann-Whitney, $P = 0.0003$). See table S5 for details on the statistical analyses.

the observed prioritization of compulsive-seeking behavior over consummatory actions (i.e., feeding) could also override other competing motivational states. To test this, we exposed mice to an unfamiliar, sex-matched mouse in a home cage environment with bedding and quantified the social interaction. In this context, activation of the D1+ ACB-LHA pathway shifted the behavior toward compulsive-like digging over social interaction (Fig. 5, I to K). Together, these findings uncover a central role for the D1+ ACB-LHA pathway in promoting and prioritizing compulsive stereotyped behaviors, even in the presence of competing high-motivation states such as hunger and social interaction.

The D1+ ACB-LHA-LHb pathway drives stereotyped behaviors in different contexts

The induction of a persistent and compulsive-like digging behavior during activation of D1+ ACB-LHA pathway motivated us to directly test the role of the downstream LHA-LHb neurons in mediating the compulsive-like induced behavior. We established an intersectional input-output strategy to optogenetically silence the LHA-LHb neurons that receive ACB inputs using NpHR (Fig. 6A and figs. S4 and S7, E and F). Similarly to the stimulation of D1+ ACB-LHA, silencing the LHA-LHb neurons receiving ACB inputs in an enriched environment shifted the behavioral repertoire and led to a significant increase in behavioral motifs associated with digging (Fig. 6, B and C; fig. S7, G and H; and table S4). To investigate whether the compulsive-like digging was a generalized form of seeking behavior that can be expressed in different contexts, we tested how optogenetic activation of the D1+ ACB-LHA pathway or silencing of the LHA-LHb neurons receiving ACB inputs affected unrewarded nose-poking behavior. In this assay, we found that the two different circuit manipulation strategies both resulted in a persistent and significant increase in nose-poking behavior in the absence of any natural reinforcer (Fig. 6, D and E), suggesting that the circuit drives a compulsive-like state characterized by stereotyped and purposeless actions. To further determine whether the nose-poking behavior was stereotyped or sensitive to motivational state and reward availability, we used a progressive ratio task. In this task, water-restricted mice were trained to nose poke in an active port to receive water rewards, with each successive reward requiring an incrementally higher number of nose pokes (fig. S7, I and J). Under baseline conditions, responding in the progressive ratio task depends on the high motivational drive (i.e., thirst) during early phases of each session and the progressively increasing effort required to obtain the reward. In contrast, we found that activation of the D1+ ACD-LHA projection resulted in a constant rate of nose poking throughout the entire session, irrespective of motivational state or response cost (fig. S7, K to N). Last, to test whether the observed compulsive-like poking behavior could be found in a different context, we used a hole-board assay to study exploration, seeking, and poking behaviors in a novel environment (Fig. 6F). We again found that the two circuit activation strategies resulted in significant

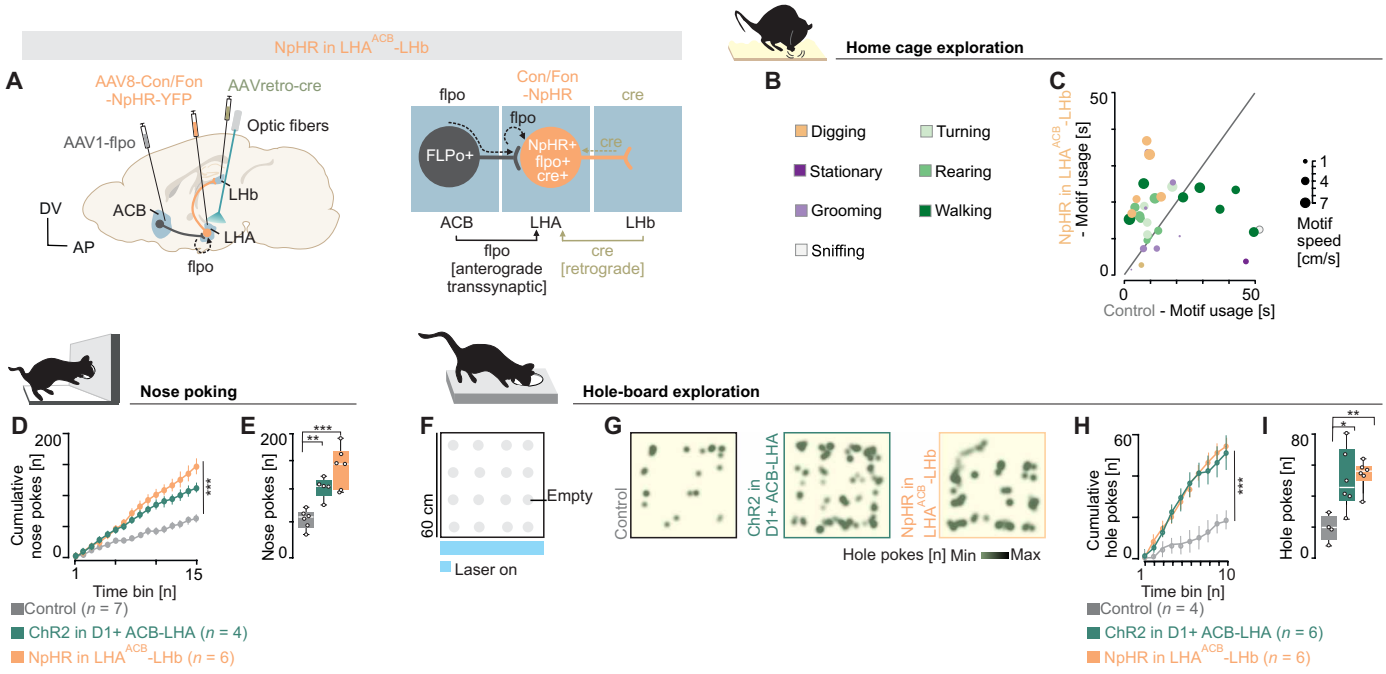

Fig. 6. The D1+ ACB-LHA-LHb pathway drives context-independent compulsive-like seeking behaviors. (**A**) Intersectional strategy for optogenetic silencing of LHA-LHb neurons receiving ACB inputs (NpHR in LHA^{ACB}-LHb). (**B** and **C**) Visualization of motif usage during optogenetic inactivation of LHA^{ACB}-LHb versus control during neutral home cage assay. Each motif is represented with a point (color, behavioral classification; size, motif speed). (**D** and **E**) Optogenetic silencing of the LHA-LHb pathway receiving ACB inputs or activation of the D1+ ACB-LHA pathway similarly increased the nose-poking behavior (two-way ANOVA, $P < 0.0001$, control versus ChR2 in D1+ ACB-LHA: $P < 0.0001$; control versus NpHR in LHA^{ACB}-LHb: $P < 0.0001$) (unpaired one-way ANOVA, $P < 0.0001$, control versus ChR2 in D1+ ACB-LHA: $P = 0.0032$; control versus NpHR in LHA^{ACB}-LHb: $P < 0.0001$). (**F**) Schematic of the hole-board assay. (**G**) Heatmaps of hole-poking in the hole-board assay. (**H** and **I**) Optogenetic silencing of the LHA-LHb pathway receiving ACB inputs or activation of the D1+ ACB-LHA pathway similarly increased the hole-poking behavior (two-way ANOVA, $P < 0.0001$, control versus ChR2 in D1+ ACB-LHA: $P < 0.0001$; control versus NpHR in LHA^{ACB}-LHb: $P < 0.0001$) (unpaired one-way ANOVA, $P = 0.0051$, control versus ChR2 in D1+ ACB-LHA: $P = 0.009$; control versus NpHR in LHA^{ACB}-LHb: $P = 0.0071$). See table S5 for details on the statistical analyses.

and sustained increase in hole poking in the absence of salient stimuli or natural rewards (e.g., food) (Fig. 6, G to I, and fig. S7, O and P). Together, these results establish that the striosomal D1+ ACB-LHA projection is a central driver of stereotyped behavioral states and acts via suppression of the downstream LHA-LHb pathway as a subcortical mechanism through which striatal circuits can override adaptive motivational control to produce compulsive-like behaviors.

DISCUSSION

Hypothalamic circuits are known to control homeostatic and innate behaviors and to play a role in motivated behaviors. The motivation to engage in specific actions is influenced by rewarding as well as aversive signals, with the LHA to LHb projection having a central function in valence processing. More specifically, glutamatergic projections from LHA that target the LHb induce strong aversion and depression-like behaviors (*15*, *17*), mediated by a neuroanatomically, molecularly, and physiologically distinct Esr1+ population in the LHA (Esr1+ LHA-LHb neurons) that shows sex-specific sensitivity in the development of stress-related states (*19*).

Here, we describe a molecularly and neuroanatomically discrete Tac1+/Oprm1+ striosomal neuron type in the ACB that directly targets Esr1+ LHA-LHb neurons. We found that activation of the ACB-LHA pathway did not induce an immediate behavioral response and instead, over repeated stimulation, induced a negative or avoidance state. We interpreted the absence of an immediate behavioral effect upon activation of the D1+ ACB-LHA pathway and the subsequent avoidance following repeated stimulation as an emerging network or plasticity mechanism that could serve to integrate circuit activity over longer timescales for the selection of behavioral programs. To test this, we stimulated the D1+ ACB-LHA pathway in different contexts to track the impact on more complex motor programs. We observed that activation of the D1+ ACB-LHA projection induced specific types of stereotyped behaviors in male and female mice, and the exact nature of those stereotyped behaviors depended on the context. For example, in an open field environment, mice exhibited increased exploratory behavior characterized by vigorous locomotion and frequent rearing. In contrast, the presence of bedding material elicited repetitive and stereotyped digging, whereas environments containing poking ports but lacking natural rewards induced persistent nose-poking behavior. We found that the D1+ ACB-LHA projection drives complex yet stereotyped digging and purposeless nose-poking behaviors even in the presence of competing natural rewards or social stimuli, indicating a shift in behavioral priority. This behavioral switch into a stereotyped mode suggests that the activation of the ACB-LHA-LHb circuit can override the motivational drive of natural rewards and promote compulsive-like behavioral programs over goal-directed actions. To ultimately uncover the mechanisms at the microcircuit, cellular, and synaptic level, which are responsible for producing stereotyped behaviors, it will be important to define the plasticity in Esr1+ LHA-LHb neurons that can mediate the shift into a stereotyped behavioral state. Examples of similar plasticity have been described in ACB synapses onto glutamatergic LHA neurons depending on the metabolic state (*21*) and in the morphine-dependent GABAergic microcircuit modulation of glutamatergic LHA neurons (*27*).

Compulsive behavior in humans is most often defined as a repetitive action performed without clear goal or intent and serving as a maladaptive strategy to transiently reduce anxiety from intrusive thoughts or obsessions (*28*). The stereotyped motor programs induced with sustained activation of striosomal ACB projections to Esr1+ LHA-LHb neurons are compulsive-like and share similarities with not only habit formation (*29*) but also the transition from goal-directed to compulsive behaviors in addiction models (*30*). Striosomes are defined by their dense localization of MORs and are recruited in drug-induced stereotyped motor programs (*31*), potentially linking striatal circuits to opioid or other substance dependence when compulsive actions persist despite negative consequences.

The role of LHA in reinforcing behaviors has been revealed through electrical self-stimulation experiments (*32*, *33*), and depending on the stimulation site in the LHA, it is possible to elicit stereotyped or compulsive-like behaviors such as grooming and digging (*34*). Supporting the role of hypothalamic circuits in the selection and structuring between behavioral programs, it has, for example, been shown that activation of Agrp-expressing neurons can override other motivational programs (*35*), and Agrp-expressing neurons can induce stereotypic actions like foraging and digging, behaviors that can be associated with food seeking or energy deficits (*12*). In addition, other hypothalamic circuits (e.g., LHA projections to PVH) control the balance between competing behaviors, such as feeding and stress-induced compulsive-like behaviors (e.g., grooming) (*36*), and galanin-expressing LHA neurons reduces compulsive marble burying whereas activation of all GABAergic LHA neurons increases this behavior (*37*). The temporal sequence of LHA-mediated behaviors shows some underlying structure, where some behavioral states tend to precede others, for example, in the case of nest building before sleep that has been linked to LHA activity, including LHA neurons with projections to LHb (*38*). These findings together highlight the broader and more complex function of hypothalamic feeding-related circuits, also offering insights into conditions defined by repetitive behaviors, such as OCD. The connection between feeding circuits and repetitive or stress-related behaviors, like marble burying, further underscores the importance of hypothalamic networks in maintaining behavioral and physiological homeostasis.

The ACB, a key component of the mesolimbic reward system, controls for aspects of motivation, reward, and compulsivity (*39*). Accumbal neurons are heterogeneous in terms of their molecular profile and projection pattern (*40*–*42*), with D1+ ACB projection neurons generally associated with promoting motivated behaviors, whereas D2+ ACB neurons linked to aversion and inhibitory control (*43*, *44*). Our results on the function of projection of D1+ ACB neurons with monosynaptic inputs to Esr1+ LHA-LHb neurons challenge the notion that D1+ neurons only promote reward-related behaviors. This agrees with evidence that D1+ neuron subtypes in the ACB can encode negative motivational valence (*45*, *46*) and spatially organized Pdyn+/D1+ subtypes drive either aversion or reward (*47*). Our findings support a more diverse function of ACB neurons, by establishing that D1+ ACB neuron subtypes with circuit-defined downstream targets can produce stereotyped and complex motor behaviors.

In summary, we describe here the identity and role of a striosomal Tac1+/Tshz1+/Oprm1+ projection from ACB that targets Esr1+ LHA-LHb neurons and drives stereotyped and compulsive-like behaviors, even in the presence of strongly competing motivational states such as feeding and social interaction. Our findings suggest that this striosome-hypothalamic-habenular circuit may be a central switch in maladaptive compulsive actions often presented in neuropsychiatric conditions such as OCD and in substance use disorders.

Together, our study contributes to a circuit-level framework for understanding the transition between flexible, goal-directed actions and compulsive behavioral states, with relevance to the neurobiology of stereotypies and compulsion in psychiatric disorders.

MATERIALS AND METHODS

Experimental design

No statistical methods were used to predetermine sample sizes, and sample sizes were similar to the published literature. Statistical hypothesis testing was conducted at a significance level of 0.05. All mice were randomly assigned to different groups. Data collection and unsupervised analysis were not performed blind to the conditions of the experiments. Behavioral tests analyses requiring manual scoring were performed by two researchers blinded to the groups. All behavioral experiments were controlled by automated computer systems/scripts (for example, ARDUINO). Mice with incorrect viral targeting or misplaced optical fiber(s) were excluded. In single-cell RNA sequencing, nuclei with less than 400 unique molecular identifiers (UMIs), or more than 100,000 UMIs, or fewer than 300 genes were excluded. The exact number of animals (*n*) for each experiment is reported in the corresponding figure legend.

Animals

All procedures and experiments on animals were performed according to the guidelines of the Stockholm Municipal Committee for animal experiments and the Karolinska Institutet in Sweden (approval number: 155440-2020). Adult mice aged 3 to 8 months were used: Esr1-cre [B6N.129S6(Cg)-Esr1tm1.1(cre)And/J; the Jackson Laboratory stock, 017911], D1-cre [B6.FVB(Cg)-Tg(Drd1-cre)EY262Gsat/Mmucd; MMRRC stock, 030989-UCD], Oprm1-ce [generated in the Meletis lab (*42*)], and wild-type mice (C57BL/6J; Charles River). Animals were group housed, up to five per cage, in a temperature-controlled (23°C) and humidity-controlled (55%) environment in standard cages on a 12-hour/12-hour light/dark cycle with ad libitum access to food and water, unless placed on a food/water restriction schedule. All food/water restricted mice were restricted to 85 to 90% of their initial body weight by administering one feeding of 2.0 to 2.5 g of standard grain-based chow per day for food restriction and 1 ml of water for water restriction. All strains used were backcrossed with the C57BL/6J strain. Male and female mice, when possible aged matched and littermates, were used for viral tracing experiments, in vivo optogenetic manipulation, and behavioral testing. The same optogenetic stimulation parameters were used in both control and experimental groups across all behavioral testing. The number of animals (*n*) for each experiment is reported at the beginning of the corresponding figure and in table S5.

Tracers and viral constructs

Purified and concentrated AAVs were purchased from Addgene: AAV1-phSyn1-FLEX-tdTomato-T2A-SypEGFP (51509-AAV1), AAV1-hSyn-Cre (105553-AAV1), AAVrg-Ef1α-fDIO-mCherry (114471-AAVrg), AAV1-EF1α-Flpo (55637-AAV1), pAAV-hSyn Con/Fon hChR2 (H134R)-EYFP (55645-AAV8), pAAV-EF1α-DIO-hChR2(H134R)-EYFP (20298-AAV5), pAAV-EF1α-DIO-hChR2(H134R)-mCherry (20297-AAV5), pAAV-EF1α-Cre (55636-AAVrg), and pAAV-nEF-Con/Fon-NpHR3.3-EYFP (137152-AAV8). HSV-EF1α-mCherry-IRES-Cre and HSV-EF1α-Flpo were obtained from the Viral Gene Transfer Core, MIT. ssAAV-DJ/2-shortCAG-dFRT-hChR2-EYFP (v237-DJ) and ssAAV-retro/2-hSyn1-dlox-TETxLC_2A_NLS_dTomato (v620-retro) were purchased from VVF Zurich. For rabies tracing, helper virus AAV-EF1α-DIO-TVA-V5 and EnvA-coated rabies viruses (RV-GFP and RV-H2B-GFP) were produced in the Meletis lab.

Stereotaxic injections

All stereotaxic injections were performed on 8- to 12-week-old mice. Mice were anesthetized with isoflurane (3% for induction, 1 to 2% for maintenance). The body temperature was maintained at 37°C using a heating pad, and ocular ointment (Viscotears, Alcon) was applied to protect the eyes. The head was fixed in a stereotaxic apparatus (Kopf), and lidocaine (4 mg/kg) was injected locally before the skin incision. After cleaning the skull with chlorhexidine, craniotomies (~300 to 500 μm) were performed. Unless otherwise specified, all injections were carried out at a speed of 100 nl/min using a glass micropipette connected to a Quintessential Stereotaxic Injector (Stoelting). ACB-LHA neurons were labeled using bilateral injections of 200 nl of cre-dependent virus [AAV1-phSyn1(S)-FLEX-tdTomato-T2A-SypEGFP-WPRE] into the ACB. The ACB was targeted using the following coordinates: 1.1 mm rostral, 0.65 mm lateral to bregma, and 3.7 mm deep from the dura.

For the neuroanatomical mapping of the ACB-LHA-LHb pathway, 200 nl of an anterograde transsynaptic Cre-expressing virus (AAV1-hSyn-Cre-WPRE-hGH; 7×10^{12} viral genomes (vg)/ml) was injected into the ACB, and a retrograde flpo-dependent mCherry-expressing virus (AAVretro-Ef1α-fDIO-mCherry) was injected into the LHb at a rate of 100 nl/min. This injection was performed unilaterally, with the LHb targeted using the coordinates: 1.65 mm caudal, 0.4 mm lateral to bregma, and 2.55 mm deep from the dura.

To visualize Esr1+-specific ACB-LHA-LHb axons, 300 nl of anterograde transsynaptic flpo-expressing virus (AAV1-EF1α-Flpo; 7×10^{12} vg/ml) was injected into the ACB, and 300 nl of cre-dependent and flpo-dependent YFP-expressing virus (AVV5-Con/Fon-ChR2-eYFP) was injected into the LHA. This injection was done unilaterally, and the LHA was targeted using the following coordinates: 1.25 mm caudal, 1 mm lateral to bregma, and 4.65 mm deep from the dura.

For optogenetic stimulation of the ACB-LHA-LHb pathway, a bilateral injection of 250 nl of anterograde transsynaptic flpo-expressing virus (AAV1-EF1α-Flpo; 7×10^{12} vg/ml) into the ACB and 250 nl of cre-dependent and flpo-dependent YFP-expressing virus (AAV8-Con/Fon-ChR2-eYFP) into the LHA was performed at a rate of 80 nl/min. To stimulate the ACB-LHA pathway, two different approaches were used: The first involved a bilateral injection of 200 nl of local cre-dependent ChR2-expressing virus [AAV5-EF1α-DIO-hChR2(H134R)-EYFP-WPRE-HGHpA] into the ACB and 200 nl of retrograde cre-expressing virus [HSV-EF1α-mCherry-IRES-Cre] into the LHA. The second approach used a bilateral injection of 200 nl of cre-dependent ChR2-expressing virus [AAV5-EF1α-DIO-hChR2(H134R)-mCherry-WPRE-HGHpA] into the ACB.

For stimulation of the ACB-LHA pathway in combination with silencing of the Esr1 LHA-LHb pathway, we established an intersectional approach using bilateral injection of 200 nl of flpo-dependent ChR2-expressing virus (AAVDJ-FRT-chR2-EYFP) into the ACB, 200 nl of retrograde flpo-expressing virus (HSV-EF1α-flpo) into the LHA, and 200 nl of retrograde cre-dependent tetanus-expressing virus [ssAAVretro/2-hSyn1-dlox-TETxLC_2A_NLS_dTomato(rev)-dlox-WPRE-hGHp(A)] into the LHb. Another approach to silence the ACB-projecting LHA-LHb pathway involved a bilateral injection of

250 nl of retrograde cre-expressing virus (AAVretro-EF1α-Cre) into the LHb, along with 250 nl of anterograde transsynaptic flpo-expressing virus (AAV1-EF1α-Flpo; 7×10^{12} vg/ml) into the ACB and 250 nl of cre-dependent and flp-dependent NpHR3.3-expressing virus (AAV8-nEF-Con/Fon-NpHR3.3-EYFP) into the LHA at a rate of 50 nl/min. Optogenetic experiments were conducted 15 days after injection. TeLC experiments were performed 4 weeks postinjection.

Across all optogenetic experiments, a similar sex and age control group was generated by injecting the same Cre-dependent or Flp-dependent vectors and implanting optic fibers at the same sites as experimental groups in wild-type mice. Post hoc anatomical analyses were performed for all animals to verify correct fiber placement and viral expression. For the rabies tracing experiment, 150 nl of helper virus (AAV-EF1α-DIO-TVA-V5-WRPE-hGHpA) was first injected into the LHA, followed 3 weeks later by injection of 150 nl of RV-GFP into the LHb at a rate of 80 nl/min. For the snRNA-seq experiment, 200 nl of the same helper virus was injected into the LHA followed 3 weeks later by injection of 200 nl of RV-H2B-GFP into the LHb (injection rate: 50 nl/min). The mice were euthanized 10 days after the injection of the RV-GFP.

For anatomical studies, mice were euthanized 3 weeks postinjection. In all stereotaxic injections, the glass pipette was left in place for 10 min postinjection before being removed from the brain. Buprenorphine [0.1 mg/kg intraperitoneally (ip)] was administered after anesthesia, before surgery, and carprofen (5 mg/kg ip) was administered immediately after surgery and 24 hours later for pain relief.

Implant surgery

Mice were anesthetized with isoflurane (3% for induction, 1 to 2% for maintenance). The body temperature was maintained at 37°C using a heating pad, and ocular ointment (Viscotears, Alcon) was applied to protect the eyes. The head was fixed in a stereotaxic apparatus (Kopf), and lidocaine (4 mg/kg) was injected locally before the skin incision. After cleaning the skull with chlorhexidine, two small craniotomies (~300 to 500 μm) were made to insert the fibers, which were lowered vertically into the brain for photoactivation [LHb: +1.65 mm anteroposterior (AP), 0.95 mm mediolateral (ML), and 2.2 mm depth, 10° angle; LHA: +1.1 mm AP, 1.2 mm ML, and 4 mm depth]. The fibers were secured with light-curing dental adhesive (OptiBond FL, Kerr) and cement (Tetric EvoFlow, Ivoclar Vivadent). Buprenorphine (0.1 mg/kg ip) was administered after anesthesia, before surgery, and carprofen (5 mg/kg ip) was administered immediately after surgery and 24 hours later for pain relief.

Immunohistochemistry

Brain sections were cut on a vibratome at 50 μm thickness (Leica VT1000, Leica Microsystems GmbH). For rabies tracing and Esr1 staining of the ACB-LHA-LHb pathway, the sections were rinsed in phosphate buffer (PB), blocked for 2 hours in 10% normal donkey serum with 0.5% Triton X-100, and then incubated overnight at 4°C with primary antibodies. The primary antibodies used were chicken anti-V5 (1:1000; Abcam, ab9113) and rabbit anti-ESRα (1:5000; Millipore, 06-935). Following extensive PB washing, sections were incubated using Cy3-conjugated and Cy5-conjugated secondary antibodies (1:1000; Jackson ImmunoResearch, 703-165-155 and 711-175-152, respectively) for 2 hours at room temperature. All antibodies were diluted in a carrier solution consisting of PB with 1% bovine serum albumin (BSA), 1% normal goat serum, and 0.5% Triton X-100. After further rinsing in PB, the sections were mounted on slides and coverslipped.

For MOR staining, sections were rinsed in TBST [tris-buffered saline (TBS) with 0.3% Triton], blocked for 1 hour in 10% donkey serum in TBS at room temperature with gentle agitation, and incubated overnight with the primary antibody rabbit anti-MOR (1:500; Abcam, ab134054) diluted in 2% donkey serum in TBST at room temperature. After washing with TBST, the sections were incubated for 2 hours at room temperature with a Cy5-conjugated secondary antibody (1:1000, same as above) diluted in 2% donkey serum in TBST. Following extensive washing with TBST and phosphate-buffered saline (PBS), the sections were mounted on slides and coverslipped.

RNAscope

The RNAscope Fluorescent Multiplex Assay V2 kit was used on rabies-GFP–expressing brain sections mounted on microscope slides. Samples were washed in 1X PBS and then treated with Pretreat 2 solution at 70° to 80°C for 5 min. After washing with distilled water and 100% ethanol, Protease3 (one drop) was added and incubated for 30 min at 40°C. Following another wash, one drop of the appropriate probe (Tac1 or A2A) was applied and incubated for 2 hours at 40°C. The sections were washed with 1X wash buffer, and one drop of AMP-1FL was added, followed by 30 min of incubation at 40°C. This procedure was repeated for AMP-2FL (15 min) and AMP-3FL (30 min). After washing with 1X wash buffer, HRP-C1 was added and incubated for 15 min at 40°C. Cy5 TSA-fluorophore (1:500) was applied and incubated for 5 min at 40°C, followed by GRP blocker for 15 min at the same temperature. Last, after a wash with 1X wash buffer, 4′,6-diamidino-2-phenylindole (DAPI) (1:1000) was applied, and the sections were coverslipped.

snRNA sequencing

To isolate brain tissue, mice were first perfused with 15 ml of the following solution: 80 mM NaCl, 75 mM sucrose, cutting/recovery solution (10x), 20 mM D-glucose (10x), and 26 mM $NaHCO_3$ (10x). Sections (300 μm) were cut using a vibratome and immediately put in an RNALater solution. The main input regions were isolated and kept in −20°C until processing for nuclei extraction. To extract nuclei, the tissue was transferred into a 2-ml tube with NP-40 lysis buffer (prepared according to the Nuclei Isolation from Complex Tissues for Single Cell Multiome ATAC + Gene Expression Sequencing protocol, CG000375) and got homogenized with the use of a two-step homogenizer. After incubation for 5 min in NP-40 lysis buffer, the homogenate was filtered through a 40-μm strainer and transferred into microcentrifuge tube to be centrifuged with 500*g* for 5 min at 4°C. After the supernatant was removed, the pellet was incubated in PBS with 1% BSA and RNA inhibitor (1 U/μl) and then resuspended. Then, this step was repeated with the same centrifuge settings and solutions. DAPI (1:1000) was added to the final solution, and it was sorted in a fluorescence-activated cell sorting (FACS) machine for the GFP signal. The collection tubes were coated with BSA beforehand. Then, the nuclei were fixed using the Parse Evercode Nuclei Fixation v3 kit. A total of ~735 nuclei were taken as input for Parse Evercode WT Evercode v3 Library preparation (using three wells of the kit). In situ nuclei barcoding, cDNA capture and amplification, and sequencing library preparation were performed according to the manufacturer's instructions, and samples were split into eight sublibraries after in situ nuclei barcoding. For both cDNA amplification and index polymerase chain reaction (PCR), eight cycles of PCR were performed, respectively. The length

distribution profile of the final library was confirmed with the Agilent Bioanalyzer, using the high-sensitivity DNA chip, yielding an average fragment size of 463 base pairs (bp). Sublibraries were pooled to a final concentration of 19.56 ng/μl, and samples were sent to Xpress Genomics AB for circularization, DNA Nanoball making, and sequencing on a MGI DNBSEQT7 Machine (PE150 kit) using Illumina TruSeq sequencing primers. The read layout was set up according to the Parse Biosciences instructions (read1: 146 bp, read2: 58 bp, index1: 8 bp, and index2: 8 bp) with stable linker sequences in the Parse barcode region being dark cycle sequenced. FASTQ files were demultiplexed into the respective sublibraries and preprocessed using the ParseBiosciences-Pipeline (v1.3.0), accounting for dark cycled bases by adding the flag "bc_amp_seq NNNNNNNNNN33333333222222222111111111" to the parfile. After preprocessing with default parameters of the Parse pipeline, 1093 cells passed initial quality control (that is, containing a full and unique parse barcode sequence). Reads were mapped to the mouse genome (mm39) using the internal version of STAR of the parse pipeline. Transcripts were annotated using gencode transcript annotations (vM31).

Image acquisition

Confocal images were captured using a Zeiss 880 confocal microscope and exported via ZEN black (2.1 SP3 v14.0). For viral expression overview, a Plan-Apochromat 10×/0.45 M27 objective was used with the following settings: frame size, 1024 by 1024; pinhole, 1.59 Airy unit (AU); bit depth, 16 bit; speed, 7; and averaging, 2. For detailed imaging of viral expression and immunohistochemistry, a Plan-Apochromat 20×/0.8 M27 objective was used with the following settings: frame size, 1024 by 1024; pinhole, 1.07 AU; bit depth, 8 bit; speed, 6; and averaging, 2. For in situ RNA quantification, a Plan-Apochromat 63×/1.40 Oil DIC M27 objective was used with the following settings: frame size, 1024 by 1024; pinhole, 0.85 AU; bit depth, 8 bit; speed, 6; and averaging, 4.

Optogenetics

Mice were bilaterally implanted with optical fibers targeting the LHb (coordinates: +1.65 mm AP, 0.95 mm ML from bregma, and 2.2 mm depth at a 10° angle from the dura) or the LHA (coordinates: +1.1 mm AP, 1.2 mm ML from bregma, and 4 mm depth from the dura). The implanted optical fibers were purchased from RWD Life Science (R-FOC-BL200C-22NA, 3 mm for LHb, 5 mm for LHA). Mice were connected via a splitter branching patch cord [SBP(2)_200/220/900-0.22_1m_FCM-2xMF1.25, Doric Lenses] to their implanted optical fibers using a split sleeve (ADAL1-5, Thorlabs). The splitter branching patch cord was connected to a laser (MLL-III-447-200 mW laser) via a fiber-optic rotary joint (FRJ_1 × 1_FC-FC, Doric Lenses) to prevent cable twisting during animal movement. The frequency and duration of photostimulation were controlled using a custom-written Arduino script (Arduino IDE), through Bonsai software (v2.6.3). For optogenetic stimulation, the light power was measured in continuous light at 8 mW at the tip of the splitter branching patch cord cable before each experiment using an optical sensor (Thorlabs). For optogenetic inhibition, power was measured in continuous light at 2 mW.

Behavioral tests

Animal handling prior to testing

All mice used in behavioral experiments were handled daily (5-min sessions) for 1 week before each test to limit stress following optic fiber connection for in vivo optogenetic experiments.

Real-time place avoidance

Mice were placed in a custom-made two-compartment behavioral arena, constructed from black plexiglass and measuring 50 cm by 25 cm by 25 cm, separated by a wall with an opening in the middle. The behavioral arena was situated on a transparent plexiglass surface, and animal behavior was recorded using a camera positioned below the arena. During habituation the optical fibers were connected to the animal without light stimulation. During the first exposure, one compartment was paired with light stimulation (40 Hz, 5-ms pulse, 447-nm laser, 10 min) followed by a second exposure in the opposite compartment (10 min). Mice were tracked using Ethovision XT 17, and the time spent in each compartment was recorded.

Elevated plus maze

Mice were placed in a custom-made behavioral arena, consisting of two open arms and two closed arms (arm width: 5 cm, arm length: 30 cm, center zone width: 5 cm, closed arms walls height: 15 cm, and elevation of the arena above the floor: 50 cm). Mice were tracked using Ethovision XT 17, and the time spent in each compartment was recorded for 10 min.

Open field

Mice were placed in a custom-made open field (30 cm by 30 cm) made of black plexiglass for 15 min. The arena was positioned on a transparent plexiglass surface to allow the camera to record behavior from below at 20 fps. Mouse performance was evaluated during alternating epochs of laser stimulation, beginning with a 5-min off period, followed by 5-min stimulation epochs (40 Hz, 5-ms pulse, 1-s on–1-s off, and 447-nm laser). Body point pose tracking and motif segmentation in the videos were performed using DLC and VAME (see Behavioral analysis for more details).

Enriched home cage

The experiment began with a prestimulation period: The mouse was placed in an empty clean cage (30 cm by 15 cm), where an optogenetic stimulation was applied for 5 min (40 Hz, 5-ms pulse, 1-s on–1-s off period, and 447-nm laser; not recorded). The mouse was then placed back in its home cage with bedding and food (pellet), where an optogenetic stimulation was applied for 5 min (40 Hz, 5-ms pulse, 1-s on–1-s off period, and 447-nm laser) (10 min, video recording from above, 20 fps). Mouse body parts were tracked using either EthoVision XT 17 or DLC. Motif classification was assessed using VAME, and digging behavior was manually scored.

Home cage exploration

The experiment began with a prestimulation period: The mouse was placed in an empty clean cage (30 cm by 15 cm), where an optogenetic stimulation was applied for 5 min (40 Hz, 5-ms pulse, 1-s on–1-s off period, and 447-nm laser; not recorded). The mouse was then placed in a clean cage with bedding, where an optogenetic stimulation was applied for 5 min (40 Hz, 5 -ms pulse, 1-s on–1-s off period, and 447-nm laser) (10 min, video recording from above, 20 fps). Mouse body parts were tracked using either EthoVision XT 17 or DLC. Motif classification was assessed using VAME.

High bedding

In a glass arena measuring 40 cm by 40 cm by 6 cm, 20 cm of sawdust bedding was placed. The experiment began with a prestimulation period: The mouse was placed in an empty clean cage (30 cm by 15 cm), where an optogenetic stimulation was applied for 5 min (40 Hz, 5-ms pulse, 1-s on–1-s off period, and 447-nm laser; not recorded). The mouse was then placed in the high bedding arena, where it was recorded for 10 min while stimulation continued.

Mouse movements were tracked using Ethovision XT 17, and digging behavior was manually scored.

Marble-burying preference

In a custom-made two-compartment behavioral arena (50 cm by 25 cm by 25 cm), one black and one white compartment were separated by a wall with a central opening. Both compartments contained a 2.5-cm layer of sawdust bedding, with no food or water present. Nine clean glass marbles (1.5 cm diameter) were placed in the black compartment. The experiment began with the mouse in a clean cage, receiving optogenetic stimulation for 5 min (40 Hz, 5-ms pulse, 1-s on–1-s off, and 447-nm laser; not recorded). After this, while stimulation continued, the mouse was placed in the arena and recorded for 10 min. At the end of the session, each mouse was returned to its cage, and the number of buried marbles was counted, with marbles considered buried if covered by sawdust by at least two-thirds. Before testing a new mouse, marbles were cleaned with 70% ethanol and placed in a freshly prepared cage. Mice were tracked using Ethovision XT 17, recording the time spent in each compartment, and discrete digging events were manually scored.

Hole board

Mice were food restricted overnight. The experiment began with the mouse being placed in an empty clean cage, where optogenetic stimulation was applied for 5 min (40 Hz, 5-ms pulse, 1-s on–1-s off period, and 447-nm laser; not recorded). Following this, the mouse was placed in an arena (45 cm by 45 cm) featuring 16 empty holes, to allow exploration of the apparatus during the first 10 min while continuing optogenetic stimulation. The holes were situated on a heightened platform, enabling hole poking. Mice were tracked using Ethovision XT 17, and discrete events of poking in the holes were manually scored.

Nose poking

Mice were placed in a 15 cm–by–15 cm box with one nose-poke port. Water delivery tubing was removed, and no reward was given. The experiment began by placing the mouse in a clean, empty cage with optogenetic stimulation (5 min, 40 Hz, 5-ms pulse, 1-s on–1-s off, and 447-nm laser). The mouse was then placed in the nose-poking box, where the number of pokes was recorded for 15 min with a custom-written Python script.

Fixed ratio

Mice were water restricted (85 to 90% of their initial body weight) and received 1 ml of water per day. Mice were trained for 4 days without optogenetic stimulation while connected to a patch cord cable. Training proceeded 15 min per day as follows: day 1, one reward per nose poke; day 2, one reward per two nose pokes; days 3 and 4, one reward per five nose pokes. On day 5, mice were tested in the progressive ratio. The number of pokes was recorded during every 15 min with a custom-written Python script.

Progressive ratio test

Mice were water restricted (85 to 90% of their initial body weight) and received 1 ml of water per day. After 4 days of training under fixed ratio to learn the association between nose poking and water delivery, mice underwent the progressive ratio test on day 5. During this test, mice received optogenetic stimulation (40 Hz, 5-ms pulse, 1-s on–1-s off, and 447-nm laser) in a clean cage starting 5 min before the test and maintained during the 15-min progressive ratio test. During testing, one reward was given for an increasing number of nose pokes, doubling the required pokes every two rewards (i.e., 1, 1, 2, 2, 4, 4, 8, 8, 16, 16, 32, 32, 64, 64, 128, and 128). The number of pokes was recorded during the 15-min test with a custom-written Python script.

Two-compartment feeding

Mice were food restricted to 85 to 90% of their initial body weight by administering one daily feeding of ~2.5 to 3.0 g of standard grain-based chow, which was given immediately following the behavioral experiment. The mice underwent food restriction for 48 hours prior to the experiment, and their weight was measured. The experiment began with the mouse being placed in an empty clean cage, where optogenetic stimulation was applied for 5 min (40 Hz, 5-ms pulse, 1-s on–1-s off period, and 447-nm laser; not recorded). Following this, food-restricted mice were placed in a custom-made two-compartment arena, consisting of a black compartment and a white compartment, separated by a wall with an opening in the middle (50 cm by 25 cm by 25 cm). Both compartments contained a 2.5-cm-thick layer of bedding to enable digging behavior. One food pellet was placed in the white compartment, and the mouse was allowed to freely consume it for 10 min while the optogenetic stimulation continued. Mice were recorded using a camera positioned above the arena and were tracked with Ethovision XT 17. Discrete events of digging and eating were manually scored.

Social interaction

Mice were single housed for 90 min prior to the test in a cage with bedding from their home cage. The experiment began by placing the mouse in a clean, empty cage for 5 min of optogenetic stimulation (40 Hz, 5-ms pulse, 1-s on–1-s off, and 447-nm laser; not recorded). The experimental mouse returned to its home cage, where a sex-matched 8-week-old mouse was introduced. Videos were recorded for 10 min and analyzed using Ethovision XT 17. Discrete events of digging and social interaction were manually scored.

Quantification and statistical analysis

Clustering of cell types in snRNA-seq

Data analysis for snRNA-seq was performed in R (v4.3.2) using the Seurat package (v5.1.0). Single nuclei were extracted from both hemispheres in five mice, resulting in 860 nuclei before filtering. The snRNA-seq data were generated using the Read10X_h5() function from Seurat. Genes related to ribosomal, mitochondrial, and X and Y chromosomes were removed, and the count matrix was filtered on the basis of reads, genes, and peaks. Low-quality nuclei and genes were filtered separately for each sample using a custom function. Doublets were removed with the DoubletFinder package (v2.0.3) using a doublet score cutoff of 0.6. RNA-seq data were normalized with SCTransform using V2 regularization, regressing out cell cycle effects based on cell cycle genes in Seurat. Harmony (group.by.vars = "sample") was applied to remove batch effects and integrate data from different samples. Clustering of the spots was done using FindNeighbors() and FindClusters() with additional parameters [dims in FindNeighbors() and pc.use in FindClusters() set to 30 PCs; resolution set to 0.4]. Uniform Manifold Approximation and Projection (UMAP) was used to visualize the clusters [FindClusters() with resolution = 0.4].

Three clusters were found with FindAllMarkers(), which was used on the SCT assay with default parameter settings to identify the markers for each cluster and were later used to assign cluster identities.

Subclustering

Data from nuclei belonging to ventral striatum were normalized using SCTransform with the same settings as those applied to the main clusters' snRNA-seq dataset. Integration of the subset was done in the same manner as the main dataset. In the mouse dataset, we selected 30 principal components (PCs) that were used in the clustering of the

subset (resolution set to 0.4), which resulted in a total of three subclusters within the ventral striatum identity.

Neuroanatomical analysis

We used the WholeBrain package in R (https://github.com/tractatus/wholebrain) to register the confocal images to the Allen reference atlas (Allen Brain Atlas CCFv2) and for segmentation of labeled neurons. Proportion of GFP-expressing neurons in brain areas was represented as means ± SEM, with individual animal data point. Starter neurons coexpressing GFP and the V5 tag were identified using immunohistochemistry with a primary antibody against V5. For MOR immunohistochemistry analysis, confocal images of sections were acquired, maintaining consistent settings across animals. For annotation of MOR+ striosomal compartments, regions of interest (ROIs) were automatically detected around MOR+ dense patches in *z*-stacks confocal images (Imaris). We used Imaris software to quantify the number of rabies-expressing neurons that colocalized Tac1 and A2A expression. Data are represented as box plots, with single animal data points.

For the axon density of ACB D1 and ACB Oprm1 terminals in the LHA, confocal microscopy images of SYP-GFP presynaptic terminals in the LHA were acquired. Acquisition settings were kept consistent across. For each brain section, image binarization, by thresholding the fluorescence level and minimum area, and pixel segmentation were performed using a custom-written script in Python. The Napari brainreg plug-in was used to register images into the Allen reference atlas (allen_mouse_10um, Allen Brain Atlas CCFv2). A Python custom-written script was used to combine the registration of brain sections with the pixel segmentation. As a result, pixel density heatmaps of the axon terminals at different AP coordinates were generated. Each heatmap represents the sum across 300 μm in the AP axes. The same strategy was adopted to visualize in the LHb the density of ChR2-YFP axon terminals from Esr1+ LHA neurons with inputs from ACB. For the ACB-LHA-LHb pathway, the number of soma in the LHA and the proportion of colocalization with the Esr1a staining was quantified manually. The Napari brainreg plug-in was used to register sample images into the Allen reference atlas (Allen Brain Atlas CCFv2). Mapping of soma position was performed using a custom-written script in Python.

Behavioral analysis

For analyzing the mouse behavior in the open field, enriched, and neutral assays, we tracked body parts using DLC and classified the actions in motifs using VAME.

Open field: Six virtual markers were placed on key body parts (nose, tail base, and paws) across 350 uniformly sampled frames from 15 videos. A residual neural network (ResNet-50) was trained to track these markers, achieving a mean error of 2.02 pixels during training and 2.49 pixels during testing. For behavioral motif identification, the unsupervised deep learning framework VAME was trained on 85 videos (1,530,000 frames) with a test fraction of 0.1, a time window of 30 frames, and a latent dimensionality of 30, converging at 50 epochs. Clustering analysis with 100 discrete states and a 1% motif usage threshold identified 41 relevant behavioral motifs within the dataset.

Enriched environment: Nine virtual markers were placed on key body parts (nose, ears, neck, shoulders, hips, and tail base) across 320 uniformly sampled frames from 16 videos. A residual neural network (ResNet-50) was trained to track these markers, achieving a mean error of 1.15 pixels during training and 6.04 pixels during testing. For behavioral motif identification, the unsupervised deep learning framework VAME was trained on 16 videos (188,800 frames) with a test fraction of 0.1, a time window of 30 frames, and a latent dimensionality of 30, converging at 50 epochs. Clustering analysis with 100 discrete states and a 1% motif usage threshold identified 39 relevant behavioral motifs within the dataset.

Neutral environment: Nine virtual markers were placed on key body parts (nose, ears, neck, shoulders, hips, and tail base) across 320 uniformly sampled frames from 16 videos. A residual neural network (ResNet-50) was trained to track these markers, achieving a mean error of 1.68 pixels during training and 5.14 pixels during testing. For behavioral motif identification, the unsupervised deep learning framework VAME was trained on 20 videos (552,000 frames) with a test fraction of 0.1, a time window of 30 frames, and a latent dimensionality of 30, converging at 50 epochs. Clustering analysis with 100 discrete states and a 1% motif usage threshold identified 41 relevant behavioral motifs within the dataset. For all VAME models, the mean motif usage in each experimental group was compared to that of the control group (Figs. 4, E and H, and 6C). Absolute motif usage values were plotted over the experimental timeline for each group of mice. A two-way analysis of variance (ANOVA) was conducted to compare experimental groups with controls. Motifs were annotated independently by two experts, and motifs were subsequently regrouped into communities based on these annotations and their behavioral classifications. For all other behavioral tests, analysis was performed using Ethovision XT 17. The Mann-Whitney *U* test was performed when comparing two independent groups. For the comparison between more than two groups, we used unpaired one-way ANOVA followed by Sidak's post hoc test. When comparing multiple groups across time, we used two-way ANOVA with repeated measures followed by Sidak's post hoc test. Discrete behaviors such as digging, eating, poking, and social interactions were manually scored. Data were presented as means ± SEM or in box plots, with individual animal data points. $*P < 0.05$; $**P < 0.01$; $***P < 0.001$.

Supplementary Materials

The PDF file includes:

Figs. S1 to S7
Tables S1 to S4
Legend for movie S1

Other Supplementary Material for this manuscript includes the following:

Movie S1

REFERENCES AND NOTES

1. G. A. Matthews, K. M. Tye, Neural mechanisms of social homeostasis. *Ann. N. Y. Acad. Sci.* **1457**, 5–25 (2019).
2. A. K. Sutton Hickey, M. J. Krashes, Integrating hunger with rival motivations. *Trends Endocrinol. Metab.* **31**, 495–507 (2020).
3. S. M. Sternson, Hypothalamic survival circuits: Blueprints for purposive behaviors. *Neuron* **77**, 810–824 (2013).
4. G. F. Koob, A role for brain stress systems in addiction. *Neuron* **59**, 11–34 (2008).
5. Y. Wang, M. Eddison, G. Fleishman, M. Weigert, S. Xu, T. Wang, K. Rokicki, C. Goina, F. E. Henry, A. L. Lemire, U. Schmidt, H. Yang, K. Svoboda, E. W. Myers, S. Saalfeld, W. Korff, S. M. Sternson, P. W. Tillberg, EASI-FISH for thick tissue defines lateral hypothalamus spatio-molecular organization. *Cell* **184**, 6361–6377.e24 (2021).
6. L. Steuernagel, B. Y. H. Lam, P. Klemm, G. K. C. Dowsett, C. A. Bauder, J. A. Tadross, T. S. Hitschfeld, A. del Rio Martin, W. Chen, A. J. de Solis, H. Fenselau, P. Davidsen, I. Cimino, S. N. Kohnke, D. Rimmington, A. P. Coll, A. Beyer, G. S. H. Yeo, J. C. Brüning, HypoMap—A unified single-cell gene expression atlas of the murine hypothalamus. *Nat. Metab.* **4**, 1402–1419 (2022).
7. H. Fong, J. Zheng, D. Kurrasch, The structural and functional complexity of the integrative hypothalamus. *Science* **382**, 388–394 (2023).

8. M. Zhang, X. Pan, W. Jung, A. R. Halpern, S. W. Eichhorn, Z. Lei, L. Cohen, K. A. Smith, B. Tasic, Z. Yao, H. Zeng, X. Zhuang, Molecularly defined and spatially resolved cell atlas of the whole mouse brain. *Nature* **624**, 343–354 (2023).
9. M. A. Rossi, Control of energy homeostasis by the lateral hypothalamic area. *Trends Neurosci.* **46**, 738–749 (2023).
10. E. H. Nieh, G. A. Matthews, S. A. Allsop, K. N. Presbrey, C. A. Leppla, R. Wichmann, R. Neve, C. P. Wildes, K. M. Tye, Decoding neural circuits that control compulsive sucrose-seeking. *Cell* **160**, 528–541 (2015).
11. J. N. Betley, S. Xu, Z. F. H. Cao, R. Gong, C. J. Magnus, Y. Yu, S. M. Sternson, Neurons for hunger and thirst transmit a negative-valence teaching signal. *Nature* **521**, 180–185 (2015).
12. M. O. Dietrich, M. R. Zimmer, J. Bober, T. L. Horvath, Hypothalamic Agrp neurons drive stereotypic behaviors beyond feeding. *Cell* **160**, 1222–1232 (2015).
13. L. E. Linders, L. Patrikiou, M. Soiza-Reilly, E. H. S. Schut, B. F. van Schaffelaar, L. Böger, I. G. Wolterink-Donselaar, M. C. M. Luijendijk, R. A. H. Adan, F. J. Meye, Stress-driven potentiation of lateral hypothalamic synapses onto ventral tegmental area dopamine neurons causes increased consumption of palatable food. *Nat. Commun.* **13**, 6898 (2022).
14. A. M. Stamatakis, M. Van Swieten, M. L. Basiri, G. A. Blair, P. Kantak, G. D. Stuber, Lateral hypothalamic area glutamatergic neurons and their projections to the lateral habenula regulate feeding and reward. *J. Neurosci.* **36**, 302–311 (2016).
15. I. Lazaridis, O. Tzortzi, M. Weglage, A. Märtin, Y. Xuan, M. Parent, Y. Johansson, J. Fuzik, D. Fürth, L. E. Fenno, C. Ramakrishnan, G. Silberberg, K. Deisseroth, M. Carlén, K. Meletis, A hypothalamus-habenula circuit controls aversion. *Mol. Psychiatry* **24**, 1351–1368 (2019).
16. S. M. Lee, H. B. Jang, Y. Fan, B. H. Lee, S. C. Kim, K. B. Bills, S. C. Steffensen, H. Y. Kim, Nociceptive stimuli activate the hypothalamus–habenula circuit to inhibit the mesolimbic reward system and cocaine-seeking behaviors. *J. Neurosci.* **42**, 9180–9192 (2022).
17. Z. Zheng, C. Guo, M. Li, L. Yang, P. Liu, X. Zhang, Y. Liu, X. Guo, S. Cao, Y. Dong, C. Zhang, M. Chen, J. Xu, H. Hu, Y. Cui, Hypothalamus-habenula potentiation encodes chronic stress experience and drives depression onset. *Neuron* **110**, 1400–1415.e6 (2022).
18. M. A. Rossi, M. L. Basiri, Y. Liu, Y. Hashikawa, K. Hashikawa, L. E. Fenno, Y. S. Kim, C. Ramakrishnan, K. Deisseroth, G. D. Stuber, Transcriptional and functional divergence in lateral hypothalamic glutamate neurons projecting to the lateral habenula and ventral tegmental area. *Neuron* **109**, 3823–3837.e6 (2021).
19. D. Calvigioni, J. Fuzik, P. Le Merre, M. Slashcheva, F. Jung, C. Ortiz, A. Lentini, V. Csillag, M. Graziano, I. Nikolakopoulou, M. Weglage, I. Lazaridis, H. Kim, I. Lenzi, H. Park, B. Reinius, M. Carlén, K. Meletis, Esr1+ hypothalamic-habenula neurons shape aversive states. *Nat. Neurosci.* **26**, 1245–1255 (2023).
20. J. H. Jennings, G. Rizzi, A. M. Stamatakis, R. L. Ung, G. D. Stuber, The inhibitory circuit architecture of the lateral hypothalamus orchestrates feeding. *Science* **341**, 1517–1521 (2013).
21. S. Thoeni, M. Loureiro, E. C. O'Connor, C. Lüscher, Depression of accumbal to lateral hypothalamic synapses gates overeating. *Neuron* **107**, 158–172.e4 (2020).
22. E. C. O'Connor, Y. Kremer, S. Lefort, M. Harada, V. Pascoli, C. Rohner, C. Lüscher, Accumbal D1R neurons projecting to lateral hypothalamus authorize feeding. *Neuron* **88**, 553–564 (2015).
23. I. R. Wickersham, D. C. Lyon, R. J. O. Barnard, T. Mori, S. Finke, K.-K. Conzelmann, J. A. T. Young, E. M. Callaway, Monosynaptic restriction of transsynaptic tracing from single, genetically targeted neurons. *Neuron* **53**, 639–647 (2007).
24. D. Fürth, T. Vaissière, O. Tzortzi, Y. Xuan, A. Märtin, I. Lazaridis, G. Spigolon, G. Fisone, R. Tomer, K. Deisseroth, M. Carlén, C. A. Miller, G. Rumbaugh, K. Meletis, An interactive framework for whole-brain maps at cellular resolution. *Nat. Neurosci.* **21**, 139–149 (2018).
25. A. Mathis, P. Mamidanna, K. M. Cury, T. Abe, V. N. Murthy, M. W. Mathis, M. Bethge, DeepLabCut: Markerless pose estimation of user-defined body parts with deep learning. *Nat. Neurosci.* **21**, 1281–1289 (2018).
26. K. Luxem, P. Mocellin, F. Fuhrmann, J. Kürsch, S. R. Miller, J. J. Palop, S. Remy, P. Bauer, Identifying behavioral structure from deep variational embeddings of animal motion. *Commun. Biol.* **5**, 1267 (2022).
27. H. Sheng, C. Lei, Y. Yuan, Y. Fu, D. Cui, L. Yang, D. Shao, Z. Cao, H. Yang, X. Guo, C. Chu, Y. Wen, Z. Cai, M. Chen, B. Lai, P. Zheng, Nucleus accumbens circuit disinhibits lateral hypothalamus glutamatergic neurons contributing to morphine withdrawal memory in male mice. *Nat. Commun.* **14**, 71 (2023).
28. T. W. Robbins, P. Banca, D. Belin, From compulsivity to compulsion: The neural basis of compulsive disorders. *Nat. Rev. Neurosci.* **25**, 313–333 (2024).
29. A. M. Graybiel, Habits, rituals, and the evaluative brain. *Annu. Rev. Neurosci.* **31**, 359–387 (2008).
30. B. J. Everitt, T. W. Robbins, Drug addiction: Updating actions to habits to compulsions ten years on. *Annu. Rev. Psychol.* **67**, 23–50 (2016).
31. J. J. Canales, A. M. Graybiel, A measure of striatal function predicts motor stereotypy. *Nat. Neurosci.* **3**, 377–383 (2000).
32. B. G. Hoebel, P. Teitelbaum, Hypothalamic control of feeding and self-stimulation. *Science* **135**, 375–377 (1962).
33. D. L. Margules, J. Olds, Identical "feeding" and "rewarding" systems in the lateral hypothalamus of rats. *Science* **135**, 374–375 (1962).
34. J. H. C. M. Lammers, W. Meelis, M. R. Kruk, A. M. van der Poel, Hypothalamic substrates for brain stimulation-induced grooming, digging and circling in the rat. *Brain Res.* **418**, 1–19 (1987).
35. C. J. Burnett, C. Li, E. Webber, E. Tsaousidou, S. Y. Xue, J. C. Brüning, M. J. Krashes, Hunger-driven motivational state competition. *Neuron* **92**, 187–201 (2016).
36. L. R. Mangieri, Y. Lu, Y. Xu, R. M. Cassidy, Y. Xu, B. R. Arenkiel, Q. Tong, A neural basis for antagonistic control of feeding and compulsive behaviors. *Nat. Commun.* **9**, 52 (2018).
37. E. Qualls-Creekmore, S. Yu, M. Francois, J. Hoang, C. Huesing, A. Bruce-Keller, D. Burk, H.-R. Berthoud, C. D. Morrison, H. Münzberg, Galanin-expressing GABA neurons in the lateral hypothalamus modulate food reward and noncompulsive locomotion. *J. Neurosci.* **37**, 6053–6065 (2017).
38. M. I. Sotelo, J. Tyan, C. Markunas, B. A. Sulaman, L. Horwitz, H. Lee, J. G. Morrow, G. Rothschild, B. Duan, A. Eban-Rothschild, Lateral hypothalamic neuronal ensembles regulate pre-sleep nest-building behavior. *Curr. Biol.* **32**, 806–822.e7 (2022).
39. S. J. Russo, E. J. Nestler, The brain reward circuitry in mood disorders. *Nat. Rev. Neurosci.* **14**, 609–625 (2013).
40. H. J. Groenewegen, F. T. Russchen, Organization of the efferent projections of the nucleus accumbens to pallidal, hypothalamic, and mesencephalic structures: A tracing and immunohistochemical study in the cat. *J. Comp. Neurol.* **223**, 347–367 (1984).
41. R. Chen, T. R. Blosser, M. N. Djekidel, J. Hao, A. Bhattacherjee, W. Chen, L. M. Tuesta, X. Zhuang, Y. Zhang, Decoding molecular and cellular heterogeneity of mouse nucleus accumbens. *Nat. Neurosci.* **24**, 1757–1771 (2021).
42. A. Märtin, D. Calvigioni, O. Tzortzi, J. Fuzik, E. Wärnberg, K. Meletis, A spatiomolecular map of the striatum. *Cell Rep.* **29**, 4320–4333.e5 (2019).
43. M. K. Lobo, H. E. Covington, D. Chaudhury, A. K. Friedman, H. Sun, D. Damez-Werno, D. M. Dietz, S. Zaman, J. W. Koo, P. J. Kennedy, E. Mouzon, M. Mogri, R. L. Neve, K. Deisseroth, M.-H. Han, E. J. Nestler, Cell type-specific loss of BDNF signaling mimics optogenetic control of cocaine reward. *Science* **330**, 385–390 (2010).
44. D. C. Castro, M. R. Bruchas, A motivational and neuropeptidergic hub: Anatomical and functional diversity within the nucleus accumbens shell. *Neuron* **102**, 529–552 (2019).
45. C. Soares-Cunha, N. A. P. de Vasconcelos, B. Coimbra, A. V. Domingues, J. M. Silva, E. Loureiro-Campos, R. Gaspar, I. Sotiropoulos, N. Sousa, A. J. Rodrigues, Nucleus accumbens medium spiny neurons subtypes signal both reward and aversion. *Mol. Psychiatry* **25**, 3241–3255 (2020).
46. J. E. Zachry, M. G. Kutlu, H. J. Yoon, M. Z. Leonard, M. Chevée, D. D. Patel, A. Gaidici, V. Kondev, K. C. Thibeault, R. Bethi, J. Tat, P. R. Melugin, A. U. Isiktas, M. E. Joffe, D. J. Cai, P. J. Conn, B. A. Grueter, E. S. Calipari, D1 and D2 medium spiny neurons in the nucleus accumbens core have distinct and valence-independent roles in learning. *Neuron* **112**, 835–849.e7 (2024).
47. R. Al-Hasani, J. G. McCall, G. Shin, A. M. Gomez, G. P. Schmitz, J. M. Bernardi, C.-O. Pyo, S. I. Park, C. M. Marcinkiewcz, N. A. Crowley, M. J. Krashes, B. B. Lowell, T. L. Kash, J. A. Rogers, M. R. Bruchas, Distinct subpopulations of nucleus accumbens dynorphin neurons drive aversion and reward. *Neuron* **87**, 1063–1077 (2015).

Acknowledgments: We thank Y. Xuan for technical assistance with rabies virus production, A. Wolthon for management of the mouse colony, and J. Frisén for use of the FACS infrastructure. We gratefully acknowledge use of the core facilities at Karolinska Institutet, specifically the animal behavior core facility (ABCF), the Biomedicum imaging facility (BIC). We acknowledge the use of the following virus constructs: AAV phSyn1(S)-FLEX-tdTomato-T2A-SypEGFP-WPRE was a gift from H. Zeng (Addgene viral prep #51509-AAV1; http://n2t.net/addgene:51509; RRID:Addgene_51509). pENN.AAV.hSyn.Cre.WPRE.hGH was a gift from J. M. Wilson (Addgene viral prep #105553-AAV1; http://n2t.net/addgene:105553; RRID:Addgene_105553). pAAV-Ef1a-fDIO mCherry was a gift from K. Deisseroth (Addgene viral prep #114471-AAVrg; http://n2t.net/addgene:114471; RRID:Addgene_114471). pAAV-EF1a-Flpo was a gift from K. Deisseroth (Addgene viral prep #55637-AAV1; http://n2t.net/addgene:55637; RRID:Addgene_55637). pAAV-hSyn Con/Fon hChR2(H134R)-EYFP was a gift from K. Deisseroth (Addgene viral prep #55645-AAV8; http://n2t.net/addgene:55645; RRID:Addgene_55645). pAAV-EF1a-double floxed-hChR2(H134R)-EYFP-WPRE-HGHpA was a gift from K. Deisseroth (Addgene viral prep #20298-AAV5; http://n2t.net/addgene:20298; RRID:Addgene_20298). pAAV-EF1a-double floxed-hChR2(H134R)-mCherry-WPRE-HGHpA was a gift from K. Deisseroth (Addgene viral prep #20297-AAV5; http://n2t.net/addgene:20297; RRID:Addgene_20297). pAAV-EF1a-Cre was a gift from K. Deisseroth (Addgene viral prep #55636-AAVrg; http://n2t.net/addgene:55636; RRID:Addgene_55636). pAAV-nEF-Con/Fon-NpHR3.3-EYFP was a gift from K. Deisseroth and INTRSECT 2.0 Project (Addgene viral prep #137152-AAV8; http://n2t.net/addgene:137152; RRID:Addgene_137152). v237 was constructed by H. Wildner, Institute of Pharmacology & Toxicology, University of Zurich, Switzerland. pAAV-hSyn-FLEX-TeLC-P2A-dTomato was a gift from S. Datta (Addgene plasmid #159102; http://n2t.net/addgene:159102; RRID:Addgene_159102). **Funding:** This research was supported by the Swedish Research Council 2018-00608 (Vetenskapsrådet MH, to K.M.), the Swedish Research Council 2023-01919 (Vetenskapsrådet MH, to D.C.), the Knut and Alice Wallenberg Foundation (KAW, grant

2020.0125, to K.M. and M.C.), the Wenner-Gren Foundation (postdoctoral funding to T.C.), the neuroscience strategic research area (StratNeuro) at Karolinska Institutet (postdoctoral funding to D.C.), and the Swedish Brain Foundation (Hjärnfonden to K.M.). **Author contributions:** T.C.: Conceptualization, data curation, formal analysis, investigation, validation, visualization, and writing—review and editing. B.Y.B.: Formal analysis, investigation, and visualization. M.G.: Data curation, formal analysis, investigation, software, and visualization. C.F.: Formal analysis, investigation, and visualization. A.C.: Data curation, formal analysis, software, and visualization. S.H.: Formal analysis and investigation. F.J.: Methodology and software. I.N.: Investigation. E.R.: Formal analysis. X.C.: Methodology and software. V.S.: Methodology and software. I.M.: Formal analysis and methodology. S.G.: Investigation. M.C.: Funding acquisition and supervision. R.S.: Resources and supervision. D.C.: Conceptualization, data curation, formal analysis, investigation, project administration, supervision, validation, visualization, writing—original draft, and writing—review and editing. K.M.: Conceptualization, funding acquisition, methodology, project administration, resources, supervision, visualization, writing—original draft, and writing—review and editing. **Competing interests:** The authors declare that they have no competing interests. **Data and materials availability:** All data needed to evaluate the conclusions in the paper are present in the paper and/or the Supplementary Materials. For behavioral experiments, single animal data points are available in main figures, supplementary figures, and supplementary tables. Source data and codes are available on Zenodo for snSEQ (https://doi.org/10.5281/zenodo.17251612) and VAME analysis (https://doi.org/10.5281/zenodo.17285222).

Submitted 4 April 2025
Accepted 24 October 2025
Published 21 November 2025
10.1126/sciadv.adx9450

ScienceAdvances

A striosomal accumbens pathway drives stereotyped behavior through an aversive Esr1+ hypothalamic-habenula circuit

Thomas Contesse, Buse Yel Bektash, Marta Graziano, Chiara Forastieri, Alessandro Contestabile, Salome Hahne, Felix Jung, Ifigeneia Nikolakopoulou, Eleonora Rubino, Xiao Cao, Vasiliki Skara, Ioannis Mantas, Sarantis Giatrellis, Marie Carlén, Rickard Sandberg, Daniela Calvigioni, and Konstantinos Meletis

Sci. Adv. **11** (47), eadx9450. DOI: 10.1126/sciadv.adx9450